

# An elasto-viscoplastic thixotropic model for fresh concrete capturing flow–rest transition

Jidu Yu<sup>a,c</sup>, Bodhinanda Chandra<sup>b,\*</sup>, Christopher Wilkes<sup>d</sup>, Jidong Zhao<sup>a</sup>, Kenichi Soga<sup>c</sup>

<sup>a</sup>*Department of Civil and Environmental Engineering, Hong Kong University of Science and Technology, Kowloon, Hong Kong*

<sup>b</sup>*Department of Mechanical Engineering, University of California, Berkeley, CA, 94720, United States*

<sup>c</sup>*Department of Civil and Environmental Engineering, University of California, Berkeley, CA, 94720, United States*

<sup>d</sup>*Ove Arup & Partners, London, United Kingdom*

---

## Abstract

The flow properties of fresh concrete are critical in the construction industry, as they directly affect casting quality and the durability of the final structure. Although non-Newtonian fluid models, such as the Bingham model, are widely used to model these flow properties, they often fail to capture key phenomena, including flow stoppage, and frequently rely on non-physical regularization or stabilization techniques to mitigate numerical instabilities at low shear rates. To address these limitations, this study proposes an elasto-viscoplastic constitutive model within the continuum mechanics framework, which treats fresh concrete as a solid-like material with a rate-dependent yield stress. The model inherently captures the transition from elastic response to viscous flow following Bingham rheology, and vice versa, enabling accurate prediction of flow cessation without ad-hoc criteria. Additionally, a thixotropy evolution law is incorporated to account for the time-dependent behavior resulting from physical flocculation and shear-induced deflocculation. The proposed model is implemented within the Material Point Method (MPM), whose Lagrangian formulation facilitates tracking of history-dependent variables and robust simulation of large deformation flows. Numerical examples demonstrate the model’s effectiveness in reproducing a range of typical concrete flow scenarios, offering a more physically consistent numerical tool for optimizing concrete construction processes and minimizing defects.

*Keywords:* Fresh concrete, Rheology, Bingham model, Elasto-viscoplasticity, Thixotropy, Material Point Method

---

\*Corresponding author

*Email address:* bchandra@berkeley.edu (Bodhinanda Chandra)

## 1. Introduction

Concrete is the most widely used construction material, which serves as a fundamental component of infrastructure development (Li et al., 2022; Environment et al., 2018). The flow behavior of fresh concrete, including its workability and flowability, critically influences the quality of placement, compaction, and finishing operations, thereby directly affecting the durability and overall performance of the structure (Roussel et al., 2007; Wallevik and Wallevik, 2011). Improper flow during casting can lead to severe defects such as honeycombing, rebar exposure, as well as flaws in concrete structure, which compromise the long-term structural integrity of the final structural element (Sun et al., 2021; Megid and Khayat, 2018; Suiker et al., 2020). As shown in Fig. 1, these defects often occur when concrete stops flowing prematurely due to factors such as thixotropy, where the material exhibits a time-dependent increase in structural strength, as well as interactions with obstacles such as reinforcement bars, mold, support fluids, and surrounding materials (Sun et al., 2024; Mahjoubi et al., 2025). Investigating the rheological properties of fresh concrete, including its workability and the mechanics behind flow interruption, is essential for developing strategies to minimize defects, optimize casting processes, and enhance the overall performance of concrete infrastructures (Wilkes et al., 2024). Furthermore, optimizing concrete mix design to improve flow properties can significantly reduce cement consumption and enhance material efficiency, contributing to lower carbon emissions and promoting greener construction practices (Nilimaa, 2023; Barbhuiya et al., 2024).

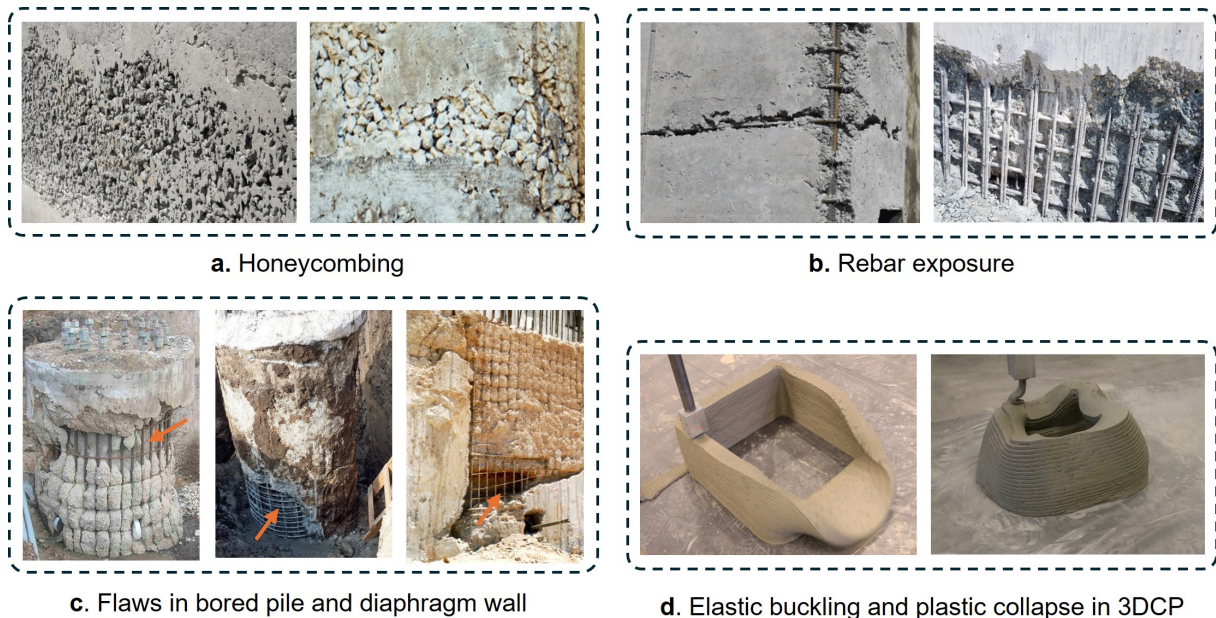


Figure 1: Typical concrete defects and flaws caused by improper casting. In Figure (d), 3DCP refers to the 3D Concrete Printing. Figures (a)-(c) are obtained from Kumar (2023); Civil Engineer Mag (2025); Desai (2025); Elop Technology (2023); Martinello (2018); Amir (2019); Figure (d) is adapted from Suiker et al. (2020).

Various mechanistic models have been proposed to describe the rheological properties of fresh concrete, with the Bingham model (Bingham, 1922) being the most widely adopted due to its simplicity and practical applicability (Deeb et al., 2014; Li et al., 2021; Yu et al., 2024a). The Bingham model treats fresh concrete as a yield-stress fluid (often referred to as a rigid-plastic fluid), assuming that the material behaves as a rigid body when the applied shear stress is below the yield stress threshold,  $\tau_0$ . Once the applied stress exceeds this threshold, the material begins to flow and the relationship between shear stress and shear rate is taken to be linear. This behavior can be expressed in terms of the shear rate as:

$$\dot{\gamma} = \begin{cases} 0, & \tau < \tau_0, \\ \frac{\tau - \tau_0}{\eta}, & \tau \geq \tau_0. \end{cases} \quad (1)$$

where  $\tau_0$  represents the critical stress required to initiate flow, while the plastic viscosity  $\eta$  governs the post-yield flow behavior.

Another commonly used model is the power-law fluid (Rao and Mishra, 2004; Manica and De Bortoli, 2004; Pichler et al., 2017), which can describe shear-thinning or shear-thickening behavior but lacks the ability to account for yield stress, making it inadequate for capturing the initiation and cessation of flow in fresh concrete. Meanwhile, the Herschel–Bulkley (HB) model (Herschel and Bulkley, 1926) extends the Bingham model's capabilities and provides a more comprehensive representation of rheological behavior by incorporating a nonlinear shear-stress–strain-rate relationship in different ranges of shear conditions (Cai et al., 2025; Li et al., 2021).

The aforementioned rheological models, in their standard form, often fail to adequately account for time-dependent effects in fresh concrete. Among those, thixotropy stands out as a key property, characterized by a reduction in viscosity under shear and a gradual recovery when the material is at rest. Thixotropy significantly influences the flowability of concrete during practical operations such as formwork filling, staged casting with sufficient time gaps between pours, or flow through congested reinforcement. In these scenarios, flocculation can restrict flow, potentially causing stoppages and leading to defects that compromise the quality of the final structure. Roussel (2006b) introduced a foundational framework that employs simplified mathematical formulations to quantify the kinetics of thixotropic behavior. In their model, a constant thixotropy coefficient  $A_{\text{thix}}$  is introduced to characterize the flocculation (i.e. structural build-up) rate of a concrete mixture, and the deflocculation (i.e. structural breakdown) term is expressed as a linear relationship of shear rate. This formulation, however, treats the effects of physical particle interactions and chemical hydration on the overall structural build-up as a single, aggregated contribution, which remains a simplification and modeling assumption (Jiao et al., 2021).

Building on Roussel's model, subsequent refined thixotropic models have been proposed to address its limitations and provide a more comprehensive description of the

structural evolution of cementitious materials. These models generally: (i) incorporate the irreversible contribution of chemical hydration, thereby decoupling it from reversible flocculation processes (Perrot et al., 2016; Lecompte and Perrot, 2017); (ii) consider the influence of multiple factors, such as the surface coverage of superplasticizer molecules, the packing density of cementitious particles, and the volume fraction of aggregate, on the flocculation rate (Mahaut et al., 2008; Lowke, 2018); and (iii) employ nonlinear laws to describe the deflocculation process, enabling the prediction of more complex shear-thinning behaviors (Wallevik, 2009; Tao et al., 2024). However, these advanced models typically require a greater number of input parameters and state variables, increasing their complexity for calibrations, and thereby, limiting their practical usability in engineering industries. Despite these advancements, Roussel (2006b)'s thixotropy model remains the most widely used in practical applications due to its ease of implementation and reduced modeling complexity (De Schryver et al., 2018; Wilkes et al., 2023).

The integration of rheological models with numerical simulation methods provides powerful tools for understanding and predicting the time-dependent flow behavior of fresh concrete under practical casting conditions. Among various numerical approaches, the mesh-based Finite Volume Method (FVM) is the most widely adopted within the concrete community. Since FVM is inherently Eulerian, it typically relies on ad hoc interface tracking techniques, such as the Volume of Fluid (VOF) method, to capture free-surface boundaries (Cai et al., 2025; Comminal et al., 2018, 2020; Shin and Kim, 2023). Through openFOAM (Jasak et al., 2007) with VOF, concrete has been modelled as a Bingham fluid (Mitchell et al., 2025) with the intent of highlighting the origin of defects related to bulk flow behaviours. However, FVM faces fundamental challenges in simulating history-dependent material behavior, such as fresh concrete with evolving thixotropic properties, due to the difficulty of tracking material state variables as they advect across a fixed grid. This, therefore, requires additional mapping procedures to properly update and transport these variables over time.

In contrast, Lagrangian-based methods, such as Smoothed Particle Hydrodynamics (SPH) (Deeb et al., 2014; Cao and Li, 2017; Ouyang et al., 2022; Yu et al., 2024a), the Lattice Boltzmann Method (LBM) (Li et al., 2021), and the Discrete Element Method (DEM) (Wu et al., 2023; Mu et al., 2023), track material motion through continuum or discrete particle representations, making them naturally suited for free-surface flows and large-deformation simulations. While these methods eliminate the need for explicit interface tracking, techniques like SPH and DEM require neighbor-search operations, which are known to be computationally demanding. Furthermore, DEM is particularly effective for representing interactions between concrete aggregates. However, because it relies solely on particle–particle contact, DEM encounters difficulties in capturing the continuous flow of cement paste, which follows a non-Newtonian constitutive response as finer grains mix with water. This limitation often necessitates coupling DEM with

a continuum solver to represent cement paste–aggregate interactions, thereby increasing model complexity and computational cost (Nan et al., 2021; Ding et al., 2025). The computational cost of DEM becomes even more significant when non-spherical aggregate geometries are considered, although recent advances in GPU computing offer promising opportunities to mitigate these challenges.

Hybrid mesh-particle methods, like the Particle Finite Element Method (PFEM) (Reinold and Meschke, 2022) and the Material Point Method (MPM) (Wilkes et al., 2023; Yildizdag, 2024), leverage the advantages of both Lagrangian particles and finite element grids, rendering them effective and accurate in simulating large deformations and free surface flows. Despite all its benefits, PFEM is generally computationally demanding as it requires frequent remeshing. By contrast, MPM employs a fixed Eulerian background grid coupled with Lagrangian material points, thereby avoiding expensive neighbor searches and remeshing while concurrently capturing history-dependent material behavior and extreme deformations. Owing to these numerical benefits, MPM has been widely applied to simulate many large-deformation problems in solids and fluids (Zhang et al., 2016; Soga et al., 2016; De Vaucorbeil et al., 2020; Yu et al., 2024b,d), including other types of viscoplastic materials, such as foams (Yue et al., 2015).

Modeling the flow behavior of fresh concrete has predominantly relied on treating it as a non-Newtonian single-phase fluid. However, this assumption presents significant limitations. A key drawback is the inherent dependence of such models on a non-zero shear strain rate to sustain shear stress, implying that the material must be continuously flowing to support shear. As a result, the material would not stop flowing unless the shear strain rate approaches zero, which is only achieved under a hydrostatic state, where the free surface becomes perpendicular to the direction of gravity. In casting simulations, this leads to unrealistic predictions in which, as time approaches infinity, the entire casting domain would eventually fill without defects. With the growing trend toward automated fabrication, particularly in 3D concrete printing, this modeling limitation becomes even more pronounced, since these approaches critically rely on the material’s ability to maintain shape after deposition. Consequently, non-Newtonian fluid models are inadequate for capturing the buildability, structural retention, and interlayer stability required in 3D printing applications. Furthermore, non-Newtonian fluid models often require numerical stabilization techniques, such as Papanastasiou regularization (Papanastasiou, 1987), to address stress discontinuities as the shear rate approaches zero. However, such stabilization introduces artificial parameters that require calibration and may lead to issues such as kinematic locking due to unrealistically high viscosities at low strain rates.

To address these limitations, this study adopts a solid-mechanics modeling approach by formulating the rheology of fresh concrete within an elasto-viscoplastic framework. Inspired by the work of Dunatunga and Kamrin (2015) for modeling of dry granular materials, this work incorporates a rate-dependent yield condition, allowing the material

to behave elastically below the yield surface and to exhibit a rate-dependent inelastic response once yielding occurs. As a result, the simulated flow naturally stops when stresses fall below the yield threshold, enabling a realistic transition to a static state (Reinold and Meschke, 2022). Moreover, the model eliminates the need for artificial stabilization techniques, providing a more physically consistent parameterization of fresh concrete behavior. Building on Roussel’s pioneering work (Roussel, 2006b), a thixotropy evolution equation is also integrated into the proposed framework. The incorporation of thixotropic mechanisms accounts for flocculation and deflocculation processes, enabling a more comprehensive representation of structural build-up with time and breakdown during flow. The proposed framework is implemented within the MPM, providing a robust and versatile computational approach for simulating fresh concrete flow under various conditions with history-dependent variables. Overall, this study aims to overcome the inherent limitations of fluid-based models and to offer a more physically consistent and predictive tool for modeling concrete processes with flow-rest transitions.

The remaining part of this paper is structured as follows. Section 2 introduces the continuum theory underlying the proposed elasto-viscoplastic model. Section 3 elaborates on the modeling framework, including a brief discussion of its implementation within the MPM and the stress update algorithm. Section 4 provides numerical examples to validate the proposed model and demonstrate its application and limitations in simulating fresh concrete flow under various conditions. Finally, Section 5 gives some concluding remarks and discusses potential directions for future research.

## 2. Theoretical framework

In this section, we present the theoretical framework for modeling fresh concrete, including the governing equations and associated constitutive assumptions. We begin by introducing the mathematical notation used throughout this work. The symbols  $\dot{\square}$  and  $\ddot{\square}$  denote first- and second-order material time derivatives, respectively. The operators  $\square \cdot \square$  and  $\square : \square$  represent the single and double tensor contractions, and  $\square \otimes \square$  denotes the tensor product. For an arbitrary second-order tensor  $\mathbf{A}$ , its trace is defined as  $\text{tr}(\mathbf{A})$ , and its deviatoric part is given by  $\mathbf{A}^* := \mathbf{A} - \text{tr}(\mathbf{A})/3$ . The symmetrization and skew-symmetrization operators are expressed as  $\text{sym}(\mathbf{A}) := (\mathbf{A} + \mathbf{A}^T)/2$  and  $\text{skw}(\mathbf{A}) := (\mathbf{A} - \mathbf{A}^T)/2$ , respectively. Throughout this study, bold or blackboard bold notation is used to denote spatial variables in tensorial form.

### 2.1. Governing equations

The conservation law of mass and momentum governs the flow of fresh concrete. In the Lagrangian description, they are given as follows,

$$\dot{\rho} + \rho \nabla \cdot \mathbf{v} = 0, \quad (2)$$

$$\rho\dot{\mathbf{v}} - \nabla \cdot \boldsymbol{\sigma} - \rho\mathbf{b} = \mathbf{0}, \quad (3)$$

where  $\rho$  is the bulk mass density,  $\mathbf{v}$  is the velocity field,  $\boldsymbol{\sigma}$  is the Cauchy stress tensor, and  $\mathbf{b}$  is the body force vector. In a boundary value problem (BVP), the objective is to solve the balance equations above with time range  $t \in [0, T]$  subjected to the following Dirichlet and Neumann boundary conditions:

$$\mathbf{v} = \hat{\mathbf{v}} \quad \text{on } \Gamma_v, \quad (4a)$$

$$\boldsymbol{\sigma} \cdot \mathbf{n} = \hat{\mathbf{t}} \quad \text{on } \Gamma_t, \quad (4b)$$

where  $\mathbf{n}$  is the outward unit normal vector, whereas  $\hat{\mathbf{v}}$  and  $\hat{\mathbf{t}}$  denote the prescribed boundary velocity and traction acting on the corresponding surfaces  $\Gamma_v$  and  $\Gamma_t$ , respectively.

## 2.2. Constitutive theory

Fresh concrete is considered to be homogenized into a single-phase continuum body that follows Bingham rheology (cf. Eq. (1)), where the material flows with a constant viscosity  $\eta$  once it is sheared beyond a certain yield stress  $\tau_0$  ( $\eta$  is often referred to as the plastic viscosity). Since concrete is a thixotropic material, its microscopic constituents flocculate at rest and deflocculate when shearing, a thixotropy-dependent variation of the yield stress should be incorporated to accurately capture its flow behavior. Instead of treating fresh concrete as a rigid–plastic fluid, in which the material is assumed rigid when the shear stress is below  $\tau_0$ , the present work models it as an elasto-viscoplastic solid. In this framework, when the stress state lies below the yield surface  $\tau_0$ , the material behaves elastically and can sustain stress. This simple shift in paradigm allows the physical cessation of material flow to be simulated, which cannot be represented by fluid models and often leads to unphysical long-term flow predictions. Further discussions comparing these two modeling approaches are provided in the subsequent section.

The total stress of the material can be decomposed into the isotropic (or volumetric) pressure and the deviatoric stress as

$$\boldsymbol{\sigma} = \boldsymbol{\tau} - p\mathbf{I}, \quad (5)$$

where  $p = -\text{tr}(\boldsymbol{\sigma})/3$  is the mean pressure (positive in compression),  $\boldsymbol{\tau}$  is the shear stress tensor (positive in tension), and  $\mathbf{I}$  is the second-order identity tensor.

The fresh concrete is assumed to behave as a weakly compressible fluid (Yu et al., 2024a). Its volumetric response can be described by the following equation of state:

$$p = \frac{\rho_0 c_0^2}{\gamma} [\exp(-\gamma\varepsilon_v) - 1], \quad (6)$$

which is a slight rewriting of the Tait–Murnaghan equation of state (see Macdonald (1966)). Here,  $\rho_0$  is the initial mass density, and  $\gamma$  is a material constant, typically chosen

as 7 to reproduce weakly compressible fluid behavior. The speed of sound in the medium is denoted as  $c_0 = \sqrt{K_0/\rho_0}$ , where  $K_0$  is the initial bulk modulus of fresh concrete.

The volumetric strain  $\varepsilon_v$  is obtained by integrating the volumetric strain rate:

$$\varepsilon_v = \int \text{tr}(\mathbf{D}) dt, \quad (7)$$

where  $\mathbf{D}$  is the strain-rate tensor, defined as the symmetric part of the velocity-gradient tensor  $\mathbf{L}$ , i.e.  $\mathbf{D} = \text{sym}(\mathbf{L})$  and  $\mathbf{L} = \nabla \mathbf{v}$ .

When flowing, the shear stress response of fresh concrete follows a generalized Newtonian fluid model (Bird et al., 1987; Chhabra and Patel, 2025), expressed as

$$\boldsymbol{\tau} = 2\eta_a \mathbf{D}^*, \quad \text{with} \quad \eta_a = \frac{\tau}{\dot{\gamma}}. \quad (8)$$

Here,  $\mathbf{D}^*$  is the deviatoric strain-rate tensor, whose norm is defined as  $\dot{\gamma} = \sqrt{2\mathbf{D}^* : \mathbf{D}^*}$ . The quantity  $\eta_a$  denotes the apparent viscosity, and  $\tau = \sqrt{J_2(\boldsymbol{\sigma})} = \sqrt{(\boldsymbol{\sigma}^* : \boldsymbol{\sigma}^*)/2}$  is the second invariant of the deviatoric stress tensor.

### 2.3. Plastic response and rheology

In the following subsections, we will elaborate further on how the deviatoric response of Bingham rheology is modeled under two frameworks: (i) the rigid-plastic fluid (with suitable regularization) and (ii) the elasto-viscoplastic solid. We also discuss how concrete thixotropy is incorporated into these models.

#### 2.3.1. Rigid-plastic Bingham fluid with regularization

Fresh concrete modeled as a Bingham fluid behaves as a rigid body before yielding and as a viscous material after yielding. However, modeling concrete as a yielding fluid is constitutively challenging, as it still requires approximating the onset of flow when  $\tau > \tau_0$ . To represent the behavior before and after yield, a commonly adopted modification of the Bingham model is the bi-viscous model (O'donovan and Tanner, 1984), which introduces a critical shear rate  $\dot{\gamma}_c$  to define the transition between the rigid and viscous regimes. The bi-viscous model is written as

$$\boldsymbol{\tau} = \begin{cases} 2\eta_0 \mathbf{D}^*, & \text{if } |\dot{\gamma}| \leq \dot{\gamma}_c, \\ 2\left(\eta + \frac{\tau_0}{\dot{\gamma}}\right) \mathbf{D}^*, & \text{otherwise,} \end{cases} \quad (9)$$

where  $\eta_0$  is the pre-yield viscosity. In practice,  $\eta_0$  is assigned a very large value to approximate the near-rigid behavior of the material in the unyielded region, effectively limiting strain rates before yielding occurs. The bi-viscous model provides a distinction between pre-yield and post-yield regions through the critical shear rate  $\dot{\gamma}_c$ ; however, the abrupt discontinuity at this transition, together with the excessively large  $\eta_0$ , often presents a computational challenge.

An alternative regularization method, which is probably the most commonly used in recent studies, involves adopting a continuous model that eliminates the distinct discontinuity between the rigid and plastic regions. The Papanastasiou (Papanastasiou, 1987) model is the most widely used among these continuous regularizations. The exponential regularization of the Bingham model, often referred to as the Bingham–Papanastasiou model, introduces a parameter  $m$  such that the shear stress is given by:

$$\tau = 2 \left[ \eta + \frac{\tau_0}{\dot{\gamma}} (1 - e^{-m\dot{\gamma}}) \right] \mathbf{D}^*. \quad (10)$$

Here, the parameter  $m$  denotes the stress growth (or regularization) parameter, which controls how rapidly the material response transitions from the pre-yield to the post-yield regime. A larger  $m$  value produces a steeper transition and more closely approximates the ideal Bingham behavior. The effect of varying  $m$  is illustrated in Fig. 2, where increasing  $m$  leads to higher apparent viscosity at low shear rates.

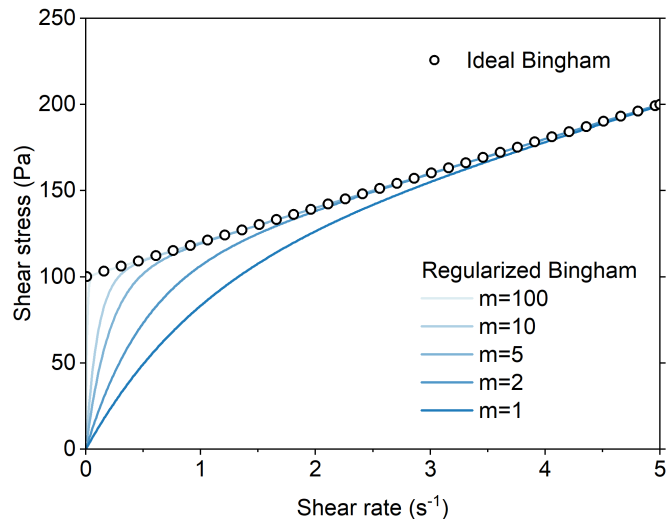


Figure 2: Stress-strain-rate relationship of the regularized Bingham model.

While the Bingham–Papanastasiou model resolves the issue of stress discontinuity, it introduces another theoretical limitation. In this formulation, the material can only sustain shear stress when it is flowing, i.e.  $\tau > 0$  if and only if  $\dot{\gamma} > 0$ . As a result, the material continues to flow indefinitely under any nonzero shear stress and can only come to rest when the shear stress vanishes, such as under lithostatic equilibrium in a gravitational-driven flow. In other words, fresh concrete materials described by this model would theoretically keep flowing over time, gradually flattening until its free surface becomes perpendicular to the direction of gravity. This “perpetual flow” behavior is physically unrealistic, since real fresh concrete can cease flowing and retain its shape once internal restructuring and thixotropic effects develop upon rest (cf. Fig. 1). This fundamental limitation motivates the adoption of an elasto-viscoplastic solid framework, enabling a

physically realistic transition to a resting state that is particularly important for long-period concrete casting simulations.

### 2.3.2. Thixotropic effect

To capture this transition to rest in a physically meaningful manner, we next introduce a thixotropy model that accounts for the time-dependent evolution of the internal structure of fresh concrete. In this work, we incorporate the thixotropy model for fresh concrete proposed by [Roussel \(2006b\)](#). This model introduces a flocculation state parameter,  $\lambda$ , which evolves over time such that the effective yield stress is expressed as

$$\tilde{\tau}_0(t) = (1 + \lambda(t))\tau_0, \quad (11)$$

where  $\tau_0$  is the reference yield stress, measured without resting time or right after mixing. The parameter  $\lambda$  characterizes the internal structural state of the material, depending on both the rest period and the experienced shear rate. When the material is at rest,  $\lambda$  increases due to particle flocculation, whereas when the material is sheared,  $\lambda$  decreases as a result of deflocculation (see Fig. 3). Flocculation increases the effective yield stress  $\tilde{\tau}_0$  because the formation of flocculated clusters enhances shearing resistance. The rate of change of  $\lambda$  can be described, following Roussel's observations, as

$$\frac{\partial \lambda}{\partial t} = \frac{A_{\text{thix}}}{\tau_0} - \alpha \lambda \dot{\gamma}, \quad (12)$$

where  $A_{\text{thix}}$  is the flocculation rate (in Pa/s) and  $\alpha$  is the deflocculation coefficient. Concrete with  $A_{\text{thix}} < 0.1$  Pa/s is typically classified as non-thixotropic, whereas concrete with  $A_{\text{thix}} > 0.5$  Pa/s is considered highly thixotropic. While the present formulation assumes a constant  $A_{\text{thix}}$ , previous studies have reported that its value may depend on the apparent shear rate ([Wallevik et al., 2015](#); [Thiedeitz et al., 2020](#)). Furthermore, the value of  $\alpha$  also plays a critical role, as it governs the exponential decrease of shear stress under a constant shear rate, with a characteristic deflocculation time scale given by  $1/(\alpha \dot{\gamma})$ . Its magnitude depends on the number and strength of interparticle links within the fresh concrete ([Assaad et al., 2003](#)). Reported values in the literature span several orders of magnitude, typically ranging from  $10^{-3}$  to  $10^{-1}$  ([Assaad et al., 2003](#); [Roussel, 2005, 2006a](#); [Qian and Kawashima, 2016](#); [Thiedeitz and Thimothy, 2024](#)).

By combining Eqs. (10), (11), and (12), we obtain the thixotropic Bingham fluid model, referred to as the Papanastasiou–Roussel Bingham (PR-Bingham) model ([Wilkes et al., 2023](#)), expressed as

$$\boldsymbol{\tau} = 2 \left[ \eta + \frac{\tau_0}{\dot{\gamma}} (1 + \lambda) (1 - e^{-m\dot{\gamma}}) \right] \boldsymbol{D}^*. \quad (13)$$

### 2.3.3. Elasto-viscoplasticity Bingham solid with thixotropy

To address the limitations of the Bingham fluid model – specifically, its inability to sustain shear stress in a non-flowing state – we model fresh concrete as an elasto-viscoplastic

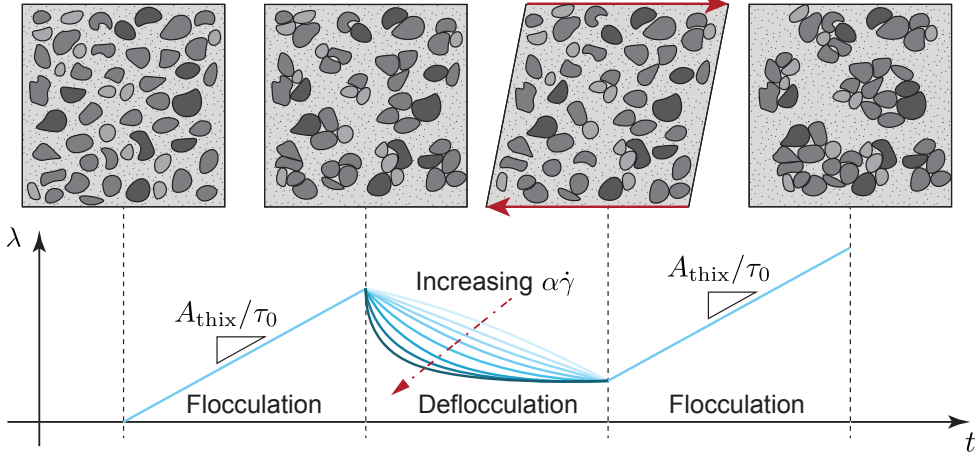


Figure 3: Schematic illustration of flocculation- and deflocculation-induced strengthening in fresh-concrete characterized through the evolution of  $\lambda$  over time.

solid following the continuum mechanics framework. In this model, the material behaves as a linear elastic solid in shear prior to yielding, with the stress state remaining below the yield threshold. Once yielding occurs, the material transitions to a viscoplastic solid, exhibiting rate-dependent dissipation characterized by the plastic viscosity  $\eta$ . This formulation inherently provides a finite stopping criterion: when the driving stress decreases below the yield threshold, the response becomes purely elastic, and inelastic deformation ceases, thereby naturally arresting the material flow.

Central to this formulation, and distinguishing it from the fluid formulation, is the additive decomposition of the strain-rate tensor  $\mathbf{D}$ , which is expressed as the sum of elastic and plastic components,  $\mathbf{D}^e$  and  $\mathbf{D}^p$ , respectively, i.e.  $\mathbf{D} = \mathbf{D}^e + \mathbf{D}^p$ . The elastic strain-rate  $\mathbf{D}^e$  represents the recoverable portion of the total strain rate that builds up elastic strain energy in the material; this strain is released once the loading is removed, resulting in elastic recovery. In contrast, the plastic strain-rate  $\mathbf{D}^p$  corresponds to the irrecoverable component of deformation, which accumulates over time and produces permanent, or inelastic, deformation of the material. Similarly, the spin-rate tensor  $\mathbf{W} = \text{skw}(\mathbf{L})$  can also be decomposed additively into its elastic and plastic parts, i.e.  $\mathbf{W} = \mathbf{W}^e + \mathbf{W}^p$ .

We define a yield surface  $f$  following the von Mises yield criterion, i.e.,

$$f = \tau - \tilde{\tau}_0, \quad (14)$$

where  $\tilde{\tau}_0$  is the effective yield stress, which may account for thixotropic effects (see Eq. (11)). During plastic flow, the yield function remains constant ( $f = 0$ ), ensuring that the stress state always lies on the yield surface; this is known as Prager's consistency condition. The plastically admissible stresses are those within the elastic domain, either inside or on the boundary of the yield surface, that satisfy the following Karush–Kuhn–Tucker

(KKT) conditions:

$$\dot{\gamma}^p f = 0, \quad \dot{\gamma}^p \geq 0, \quad f \leq 0, \quad (15)$$

where  $\dot{\gamma}^p$  denotes the equivalent plastic shear rate; this will be discussed shortly.

When the stress state lies below the yield surface ( $f < 0$ ), the material is considered to be in a solid-like state, and the stress is computed using a linear elastic model. Here, we consider elastic deformation to be fairly negligible, with its magnitude considerably smaller than that of plastic deformation, i.e.  $\mathbf{D} \approx \mathbf{D}^p$ . To ensure stress objectivity under superposed rigid motion, an objective stress rate must be employed; in this study, we adopt the Jaumann rate, i.e.,

$$\overset{\nabla}{\dot{\sigma}} \equiv \dot{\sigma} - \mathbf{W} \sigma + \sigma \mathbf{W} \approx \mathbb{C} : \mathbf{D}^e, \quad (16)$$

where the fourth-order elastic constitutive tensor is defined as

$$\mathbb{C} = K \mathbf{I} \otimes \mathbf{I} + 2G \left( \mathbb{I} - \frac{1}{3} \mathbf{I} \otimes \mathbf{I} \right), \quad (17)$$

with  $K$  and  $G$  denoting the bulk and shear moduli, respectively, and  $\mathbb{I}$  representing the fourth-order identity tensor. The bulk modulus  $K$  and  $G$  can be related to the weakly compressible fluid model defined in Eq. (6) through:

$$K = -\frac{\partial p}{\partial \varepsilon_v} = \rho_0 c_0^2 \exp(-\gamma \varepsilon_v), \quad G = \frac{3K(1-2\nu)}{2(1+\nu)}. \quad (18)$$

For fresh concrete,  $\nu$  typically ranges between 0.45 and 0.49, indicating its nearly incompressible, fluid-like nature.

Upon yielding, the plastic flow rule defines the plastic strain-rate tensor  $\mathbf{D}^p$  as proportional to the normalized deviatoric stress direction, scaled by the equivalent plastic shear rate  $\dot{\gamma}^p$ :

$$\mathbf{D}^p = \dot{\gamma}^p \frac{\boldsymbol{\tau}}{2\tau}. \quad (19)$$

Note that  $\text{tr}(\mathbf{D}^p) = 0$ ; hence,  $\mathbf{D}^p = \mathbf{D}^{p*}$  and  $\dot{\gamma}^p = \sqrt{2 \mathbf{D}^p : \mathbf{D}^p}$ . In the plastic state, where  $\dot{\gamma}^p$  is nonzero, the shear stress  $\tau$  follows the Bingham rheology, which can be extended to include the thixotropic state parameter as:

$$\tau = \eta \dot{\gamma}^p + (1 + \lambda) \tau_0. \quad (20)$$

Combining these relations, the deviatoric stress can be expressed in terms of the plastic strain rates as:

$$\boldsymbol{\tau} = 2 \left[ \eta + \frac{\tau_0}{\dot{\gamma}^p} (1 + \lambda) \right] \mathbf{D}^p. \quad (21)$$

Finally, the evolution of the flocculation state parameter  $\lambda$  can be rewritten in terms of  $\dot{\gamma}^p$  as:

$$\frac{\partial \lambda}{\partial t} = \frac{A_{\text{thix}}}{\tau_0} - \alpha \lambda \dot{\gamma}^p. \quad (22)$$

By integrating elasticity, rate-dependent plasticity, and thixotropy, the elasto-viscoplastic solid model eliminates the need for ad hoc stopping criteria and additional regularization methods. Instead, flow cessation emerges naturally when the stress state falls below the yield threshold, allowing elastic recovery to dominate while the inelastic strain rate vanishes ( $\mathbf{D}^p \rightarrow 0$ ). Meanwhile, the thixotropic term gradually increases the yield stress over time, making the material progressively more resistant to yielding and thereby aligning the framework with experimentally observed fluid-solid transitions in fresh concrete flow.

### 3. Modeling framework and discretization

#### 3.1. Material point discretization

In this work, we employ the Material Point Method (MPM) (Sulsky et al., 1994), a continuum simulation technique derived from the Fluid–Implicit–Particle (FLIP) method (Brackbill and Ruppel, 1986) for modeling large-deformation continua. In MPM, the body is discretized into Lagrangian material points that store history-dependent variables of the continuum, while a background Eulerian grid is used to solve the governing equations of motion. Because all state information is carried by the material points, the background mesh can be reset at the beginning of each time step without any loss of information, allowing the method to handle large deformations without introducing errors associated with mesh distortion. A schematic of the MPM cycle is shown in Fig. 4.

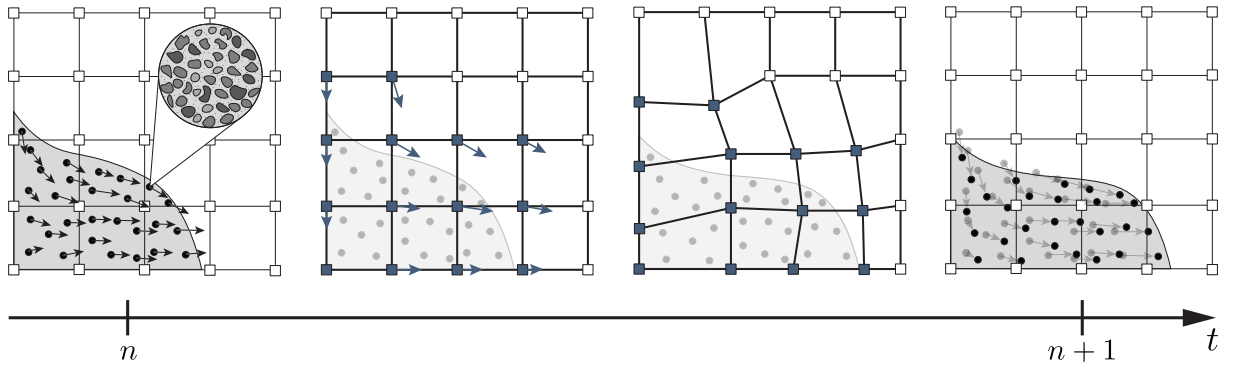


Figure 4: MPM computational cycle at each time step. In the MPM, a continuum body is discretized into a set of material points that move spatially. A material point is not a real physical particle, but rather a control volume representing a homogenized portion of the material domain. At the beginning of each time step, the kinematic fields are mapped from the material points to a background grid (with active nodes highlighted in blue). The next step is to solve the mass and momentum balance equations, considering imposed boundary conditions. At the end of the step, the kinematic fields are transferred back to the material points, where they are then advected through space. After deformation, the background grid can be reset to its original shape.

The MPM framework follows a variational formulation based on the Bubnov–Galerkin

method. The weak form of the momentum balance equation (Eq. (3)) can be written as:

$$\int_{\Omega} \delta \mathbf{u} \cdot \rho \ddot{\mathbf{u}} d\Omega + \int_{\Omega} \nabla \delta \mathbf{u} : \boldsymbol{\sigma} d\Omega - \int_{\Omega} \delta \mathbf{u} \cdot \rho \mathbf{b} d\Omega - \int_{\Gamma_t} \delta \mathbf{u} \cdot \bar{\mathbf{t}} d\Gamma = 0, \quad (23)$$

where  $\delta \mathbf{u}$  denotes an arbitrary test function. Using finite element discretization, the displacement field and its corresponding test function are approximated as

$$\mathbf{u}(\mathbf{x}) = \sum_{I=1}^{n_n} S_I(\mathbf{x}) \mathbf{u}_I, \quad \delta \mathbf{u}(\mathbf{x}) = \sum_{I=1}^{n_n} S_I(\mathbf{x}) \delta \mathbf{u}_I, \quad (24)$$

where  $n_n$  is the total number of nodes and  $S_I$  is the shape function associated with node  $I$  in the background grid. Employing this approach and invoking the arbitrariness of the test function, we can discretize the momentum balance equation and solve for the nodal acceleration  $\mathbf{a}_J^{n+1}$  at time  $t = n + 1$  as:

$$m_I^n \mathbf{a}_I^{n+1} = \mathbf{f}_I^{\text{int},n} + \mathbf{f}_I^{\text{ext},n}, \quad (25)$$

where the nodal mass  $m_I$ , internal force  $\mathbf{f}_I^{\text{int}}$ , and external force  $\mathbf{f}_I^{\text{ext}}$  are defined as:

$$m_I^n = \sum_{p=1}^{n_p} S_I(\mathbf{x}_p) m_p, \quad (26)$$

$$\mathbf{f}_I^{\text{int},n} = - \sum_{p=1}^{n_p} \nabla S_I(\mathbf{x}_p) \cdot \boldsymbol{\sigma}_p^n V_p^{n+1}, \quad (27)$$

$$\mathbf{f}_I^{\text{ext},n} = \sum_{p=1}^{n_p} S_I(\mathbf{x}_p) \mathbf{b}_p m_p + \int_{\Gamma_t} S_I(\mathbf{x}) \bar{\mathbf{t}}(\mathbf{x}) d\Gamma. \quad (28)$$

In the notation above, the variables at grid nodes are indicated with subscript  $I$ , whereas subscript  $p$  denotes material point variables. The total number of material points located within the local neighborhood of  $I$  is indicated by  $n_p$ . Here,  $m_p$  and  $V_p$  denote the material point mass and volume, respectively. Notice that the traction surface integral in Eq. (28) is left in its weak form for now as its discretization is non-trivial due to boundary nonconformity, see (Bing et al., 2019; Chandra et al., 2021; Liang et al., 2023) for more details.

### 3.2. Stress update algorithms

The implementation of the two Bingham models requires prior knowledge of the strain-rate tensor, which can be approximated through the MPM discretization. At the start of each compute step, the strain-rate tensor at a material point can be calculated as

$$\mathbf{D}_p^{n+1} = \text{sym}(\mathbf{L}_p^{n+1}), \quad \text{where} \quad \mathbf{L}_p^{n+1} = \sum_{I=1}^{n_n} \nabla S_I(\mathbf{x}_p) \otimes \mathbf{v}_I^n. \quad (29)$$

Here,  $\mathbf{v}_I^n$  denotes the nodal velocities interpolated from the particles during the P2G (particle-to-grid) mapping. The velocity-gradient tensor is also used to update the material point volume, according to:

$$V_p^{n+1} = \Delta J_p V_p^n, \quad \text{where} \quad \Delta J_p = 1 + \text{tr}(\mathbf{L}_p^{n+1})\Delta t, \quad (30)$$

and  $\Delta t$  is the time-step increment, which must be sufficiently small to satisfy the Courant–Friedrichs–Lowy (CFL) condition for explicit time integration.

### 3.2.1. Papanastasiou–Roussel Bingham fluid model

Following the computation of the strain-rate tensor  $\mathbf{D}^{n+1}$ , the stress update for the PR-Bingham fluid model can be carried out explicitly at each material point following the classical hydrodynamics framework. For simplicity, the subscript  $p$  is omitted hereafter, as all quantities are assumed to be material point properties.

First, by evaluating the initial sound speed  $c_0 = \sqrt{K_0/\rho_0}$ , the updated pressure  $p^{n+1}$  can be computed using the weakly compressible equation of state previously given by Eq. (6), which governs the volumetric response of the material, i.e.,

$$p^{n+1} = \frac{\rho_0 c_0^2}{\gamma} [\exp(-\gamma \varepsilon_v^{n+1}) - 1], \quad \text{where} \quad \varepsilon_v^{n+1} = \frac{V^{n+1}}{V_0} - 1. \quad (31)$$

Here,  $V_0$  is the initial volume of the material point.

For the deviatoric response, the deviatoric component of the strain-rate tensor is used to compute the equivalent shear rate,

$$\dot{\gamma}^{n+1} = \sqrt{2\mathbf{D}^{*,n+1} : \mathbf{D}^{*,n+1}}. \quad (32)$$

This shear rate is then used to update the flocculation state parameter via a forward Euler time-integration scheme,

$$\lambda^{n+1} = \lambda^n + \left( \frac{A_{\text{thix}}}{\tau_0} - \alpha \lambda^n \dot{\gamma}^{n+1} \right) \Delta t. \quad (33)$$

The initial value of the flocculation state  $\lambda = \lambda_0$  should be assigned at the beginning of the time step, which can be determined either from rest time or direct experimental measurements. With the updated flocculation parameter, the deviatoric stress tensor  $\boldsymbol{\tau}^{n+1}$  is then computed from the apparent viscosity and strain rates as:

$$\boldsymbol{\tau}^{n+1} = 2 \left[ \eta + \frac{\tau_0}{\dot{\gamma}} (1 + \lambda^{n+1}) (1 - e^{-m\dot{\gamma}^{n+1}}) \right] \mathbf{D}^{*,n+1}. \quad (34)$$

Finally, the total Cauchy stress is assembled by combining the deviatoric and isotropic components,

$$\boldsymbol{\sigma}^{n+1} = \boldsymbol{\tau}^{n+1} - p^{n+1} \mathbf{I}. \quad (35)$$

**Remark 1.** In the current study, we do not consider splitting the thixotropy evolution according to a critical shear rate,  $\dot{\gamma}_c$ , which is often employed to distinguish between the resting and flowing states of a material, such that regions with  $\dot{\gamma} < \dot{\gamma}_c$  are treated as being at rest (e.g., [Beverly and Tanner \(1992\)](#)). Following this approach, as demonstrated by [Wilkes et al. \(2023\)](#), thixotropic structuration is assumed to occur only in these resting states, whereas destructureation occurs only during the flowing states, i.e.  $\dot{\gamma} > \dot{\gamma}_c$ . In contrast to their approach, the current model allows the thixotropy parameter to evolve, both structuration and destructureation, continuously, thereby eliminating the need for an explicit definition of a shear-rate threshold.

### 3.2.2. Elasto-viscoplastic Bingham model with thixotropy

According to the theory established in Section 2.3.3, the stress-update algorithm of the elasto-viscoplastic model can be summarized as

$$\boldsymbol{\sigma}^{n+1} = \boldsymbol{\sigma}^n + \Delta t \left( \mathbb{C} : (\mathbf{D}^{n+1} - \mathbf{D}^{p,n+1}) + \mathbf{W}^{n+1} \boldsymbol{\sigma}^n - \boldsymbol{\sigma}^n \mathbf{W}^{n+1} \right). \quad (36)$$

Here, the strain-rate tensor and the spin tensor are computed following Eq. (29), with  $\mathbf{W}^{n+1} = \text{skw}(\mathbf{L}^{n+1})$ . The unknown in this expression is the plastic strain-rate tensor  $\mathbf{D}^{p,n+1}$ , whose value is zero for purely elastic deformation and nonzero otherwise, cf. Eqs. (15) and (19).

The stress update procedure follows a predictor–corrector plastic flow formulation, in which a trial stress state  $\boldsymbol{\sigma}^{tr}$  is first computed under the assumption of fully elastic deformation. If the trial stress lies within the yield surface, it is accepted as the solution for the next step. Conversely, if the trial stress state exceeds the yield surface, a radial return-mapping algorithm is invoked based on the flow rule given in Eq. (19). In addition, the evolution of the thixotropic state parameter  $\lambda$  should be updated concurrently during the return-mapping process, which correspondingly causes the evolution of the yield surface  $\tilde{\tau}_0$  with time and during plastic shearing.

The trial stress  $\boldsymbol{\sigma}^{tr}$  can be computed as:

$$\boldsymbol{\sigma}^{tr} = \boldsymbol{\sigma}^n + \Delta t \left( \mathbb{C} : \mathbf{D}^{n+1} + \mathbf{W}^{n+1} \boldsymbol{\sigma}^n - \boldsymbol{\sigma}^n \mathbf{W}^{n+1} \right). \quad (37)$$

Here, we consider a rotationally-neutralized stress update algorithm to ensure objectivity, as suggested by [Simo and Hughes \(2006\)](#). Considering that the motion is entirely elastic, we also compute the trial thixotropy state parameter  $\lambda^{tr}$  by setting  $\dot{\gamma}^p = 0$ , i.e.,

$$\lambda^{tr} = \lambda^n + \frac{A_{\text{thix}}}{\tau_0} \Delta t. \quad (38)$$

Here, only the flocculation rate is considered, as the structural build-up is a solely time-dependent function.

Once the trial stress and thixotropy state are obtained, the trial yield function  $f^{tr}$  can be evaluated following Eq. (14), i.e.,

$$f^{tr} = f(\boldsymbol{\sigma}^{tr}, \lambda^{tr}) = \tau^{tr} - (1 + \lambda^{tr})\tau_0, \quad (39)$$

where  $\tau^{tr}$  is the deviatoric stress invariant corresponding to  $\boldsymbol{\sigma}^{tr}$ . If  $f^{tr} \leq 0$ , the trial stress lies within the elastic domain and is therefore accepted as an admissible stress state. We then set  $\boldsymbol{\sigma}^{n+1} = \boldsymbol{\sigma}^{tr}$ ,  $\lambda^{n+1} = \lambda^{tr}$ , and  $\dot{\gamma}^{p,n+1} = 0$ , accordingly.

Meanwhile, if  $f^{tr} > 0$ , the stress lies above the yield surface (see Fig. 5), and thus a return-mapping algorithm is required to bring the stress state back to the yield surface, i.e.  $f(\boldsymbol{\sigma}^{n+1}, \lambda^{n+1}, \dot{\gamma}^{p,n+1}) \rightarrow 0$ . However, due to thixotropy evolution, the yield surface may soften according to the deflocculation term arising from plastic shearing (see the second term in Eq. (12)). These conditions can be satisfied by minimizing the following set of equations:

$$\boldsymbol{\sigma}^{n+1} - \boldsymbol{\sigma}^{tr} + \Delta t \mathbb{C} : \mathbf{D}^{p,n+1} = \mathbf{0}, \quad (40)$$

$$\lambda^{n+1} - \lambda^{tr} + \Delta t \alpha \dot{\gamma}^{p,n+1} \lambda^{n+1} = 0. \quad (41)$$

Here, note that  $\dot{\gamma}^{p,n+1} > 0$ , and consequently  $\mathbf{D}^{p,n+1} \neq \mathbf{0}$ , as previously stated by the yield condition in Eq. (15) and the plastic flow rule in Eq. (19).

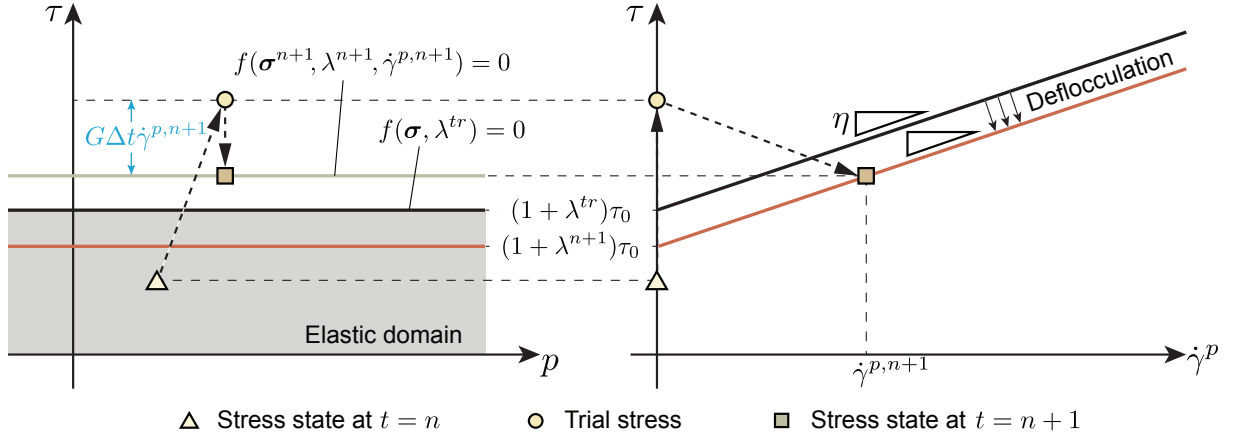


Figure 5: Schematic illustration of the proposed stress return mapping algorithm in  $\tau$ - $p$  space and  $\tau$ - $\dot{\gamma}^p$  space.

As the adopted plastic flow rule is purely deviatoric (or isochoric), meaning no volumetric plastic deformation is considered, the updated pressure can be directly set as  $p^{n+1} = p^{tr}$ . Therefore, only the deviatoric stress needs to be computed through the return-mapping process. By taking the deviatoric invariant of Eq. (40) and performing some algebraic manipulation, Eqs. (40) and (41) can be reduced to a single residual equation:

$$\tau^{tr} - (\Delta t G + \eta) \dot{\gamma}^{p,n+1} - \tau_0 \left( 1 + \frac{\lambda^{tr}}{1 + \alpha \dot{\gamma}^{p,n+1} \Delta t} \right) = 0. \quad (42)$$

Taking the positive root of  $\dot{\gamma}^{p,n+1}$ , we can obtain the closed-form expression:

$$\dot{\gamma}^{p,n+1} = \frac{\sqrt{\xi^2 + 2\zeta f^{tr}} - \xi}{\zeta}, \quad (43)$$

where the constants  $\xi$  and  $\zeta$  are:

$$\xi = \eta + \Delta t (G + \alpha(\tau_0 - \tau^{tr})) , \quad \zeta = 2\alpha \Delta t (\Delta t G + \eta) . \quad (44)$$

Once the plastic shear strain rate is obtained, the deviatoric stress invariant and the thixotropy state parameter can be updated as:

$$\tau^{n+1} = \tau^{tr} - \Delta t G \dot{\gamma}^{p,n+1} , \quad \lambda^{n+1} = \frac{\lambda^{tr}}{(1 + \Delta t \alpha \dot{\gamma}^{p,n+1})} . \quad (45)$$

Lastly, the total Cauchy stress can be assembled considering the co-directionality of the trial and updated deviatoric stresses, and thus,

$$\boldsymbol{\sigma}^{n+1} = \frac{\tau^{n+1}}{\tau^{tr}} \boldsymbol{\tau}^{tr} - p^{n+1} \mathbf{I} . \quad (46)$$

**Remark 2.** It is worth noting that Eq. (43) is derived under the assumption that  $\lambda$  varies with the plastic shear strain rate  $\dot{\gamma}^p$ , i.e. when  $\alpha > 0$ . When  $\alpha = 0$ , corresponding to a non-thixotropic material, the denominator  $\zeta = 0$ , resulting in Eq. (43) being undefined. In this case, the correct procedure is to set  $\alpha = 0$  directly in Eq. (42). This reduces the residual to a linear equation, leading to the explicit solution if  $\alpha = 0$ :

$$\dot{\gamma}^{p,n+1} = \frac{f^{tr}}{\eta + \Delta t G} . \quad (47)$$

### 3.3. Verification test: planar Poiseuille flow

To verify the proposed formulation and implementation, we conducted a one-dimensional Poiseuille flow simulation between parallel plates. The geometry of the problem is shown in Fig. 6a, where a Bingham fluid is confined between two parallel plates with no-slip boundaries. A horizontal body force per unit volume,  $F$ , is applied to drive the flow until a steady-state condition is reached. To obtain a unique steady-state solution, the thixotropic model is disabled by keeping the thixotropy parameter unchanged, that is  $\lambda = 0$  and  $\partial\lambda/\partial t = 0$  throughout the simulation. The steady-state horizontal velocity solution is given for  $y \in (-H/2, H/2)$  as (Bird, 2002):

$$v_x = \begin{cases} \hat{v}_x(y_0), & |y| \leq y_0 , \\ \hat{v}_x(|y|), & y_0 < |y| \leq \frac{H}{2} , \end{cases} \quad (48)$$

where the boundary between the yielding and non-yielding regions is defined by  $y_0 = \tau_0/F$ . The velocity profile of the yielded region is

$$\hat{v}_x(|y|) = \frac{1}{2\eta} \left[ F \left( \frac{H^2}{4} - y^2 \right) - 2\tau_0 \left( \frac{H}{2} - |y| \right) \right] . \quad (49)$$

Meanwhile, the *plug-region* velocity is constant and equal to:

$$\hat{v}_x(y_0) = \frac{1}{2\eta} \left[ F \left( \frac{H^2}{4} - y_0^2 \right) - 2\tau_0 \left( \frac{H}{2} - y_0 \right) \right]. \quad (50)$$

The material and loading parameters used in this verification test are: the yield stress is considered to vary  $\tau_0 = \{10, 50, 100, 200\}$  Pa, mass density  $\rho = 2000$  kg/m<sup>3</sup>, body force  $F = 2000$  N/m<sup>3</sup>, channel height  $H = 0.5$  m, and dynamic viscosity  $\eta = 30$  Pa·s. For the Papanastasiou Bingham model, the regularization parameter is set as  $m = 10$ . The initial bulk modulus is  $K_0 = 0.33$  MPa, and the Poisson ratio is  $\nu = 0.45$ . The simulation is performed using MPM with periodic boundary conditions along the sides, 16 particles per cell, and a cell size of 0.01 m. The scheme and other numerical settings follow those described in Section 4. The simulation results from both the Papanastasiou Bingham model and the elasto-viscoplastic model are shown in Fig. 6b, where the characteristic plug flow at the channel center is accurately reproduced. In this study, we aim to verify and show that the proposed framework and implementation match the Bingham fluid model in the steady-state flowing limit and even provide better accuracy in representing the plug velocity field, where the shear strain rate should be exactly zero.

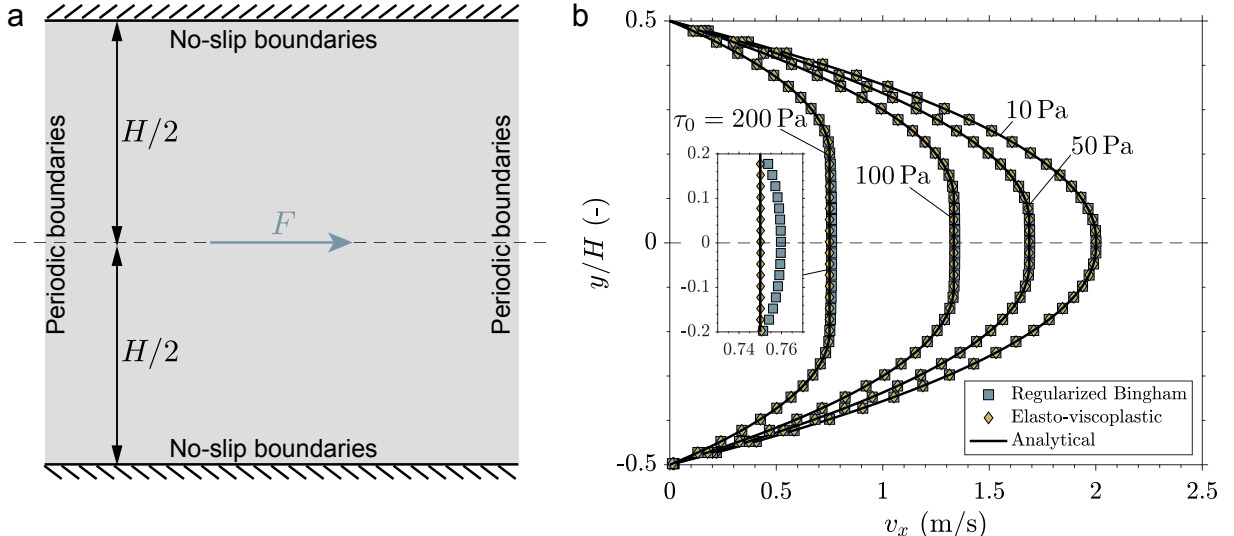


Figure 6: Planar Poiseuille flow: (a) Model geometry and (b) obtained numerical results utilizing the Papanastasiou-regularized and elasto-viscoplastic Bingham model in comparison with analytical solutions. The inset plot shows a zoomed view of the plug velocity field with  $\tau_0 = 200$  Pa.

#### 4. Numerical examples

In this section, we rigorously validate the proposed model against several common on-site testing procedures for fresh concrete. We first conducted a series of slump flow tests (BSI, 2019) with three primary objectives: (1) to evaluate whether the proposed elasto-viscoplastic model, stress-integration algorithm, and MPM implementation can accurately

capture the flow–rest transition of fresh concrete and the resulting slump flow distance; (2) to assess the capability of the model in reproducing the dynamic flow process; and (3) to verify whether the proposed thixotropic model can consistently simulate the thixotropic behavior of concrete, including the rheological response after different rest times. Finally, we simulated two additional standard tests, the L-box test and the V-funnel test, to further assess the model’s capability in predicting flow interacting with reinforcing bars and in capturing flow under channelized geometries.

In all MPM simulations presented in this section, we employ the explicit MPM formulation with linear shape functions and three-dimensional structured hexahedral elements. To ensure numerical stability and mitigate volumetric locking under nearly incompressible conditions, we adopt the MUSL (Modified Update Stress Last) scheme (Nairn, 2003) together with the B-bar method (Hughes, 1980). For particle velocity updates, the FLIP (FLuid Implicit Particle) scheme (Brackbill and Ruppel, 1986) is used to maintain energy conservation. The current MPM implementation and framework are available open source on GitHub<sup>1</sup>, and have been extensively developed and validated for a wide range of solid, geomechanics, and fluid mechanics applications (Kularathna et al., 2021; Liang et al., 2022; Chandra et al., 2024a,b; Kurima et al., 2025).

#### 4.1. Slump flow test

The slump flow test is widely adopted as an on-site method to assess the workability and flow characteristics of fresh concrete, particularly self-compacting and Tremie concrete mixes (Domone, 1998; Roussel et al., 2016a; Wilkes et al., 2023). It provides a practical and straightforward field test to quantify concrete flowability by measuring the final slump flow diameter (denoted as SF) after the standard cone is lifted. For Tremie concrete, which is essential in deep foundation applications such as diaphragm walls and bored piles, maintaining high fluidity is crucial to ensure proper flow around reinforcement cages and through pipes without segregation. In this study, three sets of slump flow simulations are conducted, each designed with a specific objective.

##### 4.1.1. Roussel’s benchmark test

Roussel’s slump flow test is a well-known benchmark for evaluating numerical models of fresh concrete flow (Roussel et al., 2016a) across different numerical simulators. The test is based on the standard Abrams cone geometry, with initial dimensions  $H_0 = 300$  mm,  $R_{\min} = 50$  mm, and  $R_{\max} = 100$  mm, as shown in Fig. 7a. The fresh concrete is modeled as a homogeneous Bingham material characterized by a yield stress  $\tau_0 = 50$  Pa, plastic viscosity  $\eta = 50$  Pa·s, mass density  $\rho = 2300$  kg/m<sup>3</sup>, and gravitational acceleration  $g = 9.81$  m/s<sup>2</sup>. The analytical solution for the final slump flow diameter is derived under the

---

<sup>1</sup><https://github.com/geomechanics/mpm>

following assumptions (Roussel and Coussot, 2005): (1) inertia and surface tension effects are neglected; (2) the flow regime is quasi-static; and (3) the problem is simplified to a one-dimensional flow profile in the regime  $H \ll R$  with a mono-dimensional yielding criterion where flow ceases once the shear stress equals the yield stress. Here,  $H$  and  $R$  are the final height and radius of the specimen. The final surface profile is expressed as:

$$h(r) = \frac{2\tau_0}{\rho g}(R - r), \quad R = \left( \frac{225\rho g \Omega^2}{128\pi^2 \tau_0} \right)^{1/5}, \quad (51)$$

where  $h(r)$  is the height or thickness of the concrete at radial distance  $r$  and  $\Omega$  is the specimen volume (can be taken as its initial value). The effect of thixotropy is not considered in this benchmark test.

In the MPM simulation, a no-slip boundary condition is applied at the flat base, while the influence of the cylindrical container surrounding the concrete is neglected (Reinold and Meschke, 2022). The initial material points are generated using an unstructured distribution, where tetrahedral elements are first created with `Gmsh` (Geuzaine and Remacle, 2009). A material point is then placed at the centroid of each tetrahedron, and its volume is assigned to match that of the corresponding element. The simulation contains a total of 24,027 material points, and the background mesh consists of a structured hexahedral grid with a cell size of 10 mm. The elastic parameters are taken as Young's modulus  $E_0 = 100$  kPa and Poisson's ratio  $\nu = 0.3$  following Reinold and Meschke (2022)<sup>2</sup>. The time step is set to  $5 \times 10^{-4}$  s.

Fig. 7c presents the simulation results of the slump flow test at different time instants using the elasto-viscoplastic model, while Fig. 7d shows the final concrete profile, with the colored contour representing the equivalent plastic strain. For comparison, the simulation results by PFEM reported in Reinold and Meschke (2022) are also presented in Fig. 7b (only a quarter of the domain is simulated). It can be observed that the slump flow shapes predicted by both MPM and PFEM are quite similar. Both our simulation and the PFEM simulation exhibit a crowning-like region around  $t = 0.5$  s, indicating a circular plug zone undergoing rigid-body motion with no plastic shear strain. In Fig. 7e, a further comparison is made between the simulated final slump flow diameter and the analytical solution. The results indicate that the MPM simulation based on the elasto-viscoplastic model stabilizes after 10 s, and the final value agrees very well with the analytical solution. In contrast, the MPM simulation using the regularized Bingham fluid model shows a continuous increase in the slump flow diameter, eventually exceeding the analytical prediction. Additionally, the PFEM results based on a hyperelastic-viscoplastic model can also capture the stoppage of the flow, though the simulated values appear to be smaller than the analytical solution

---

<sup>2</sup>Knowing Young's modulus and the Poisson ratio, one may compute the initial bulk modulus  $K_0$  required for the volumetric response (cf. Eq. (6)).

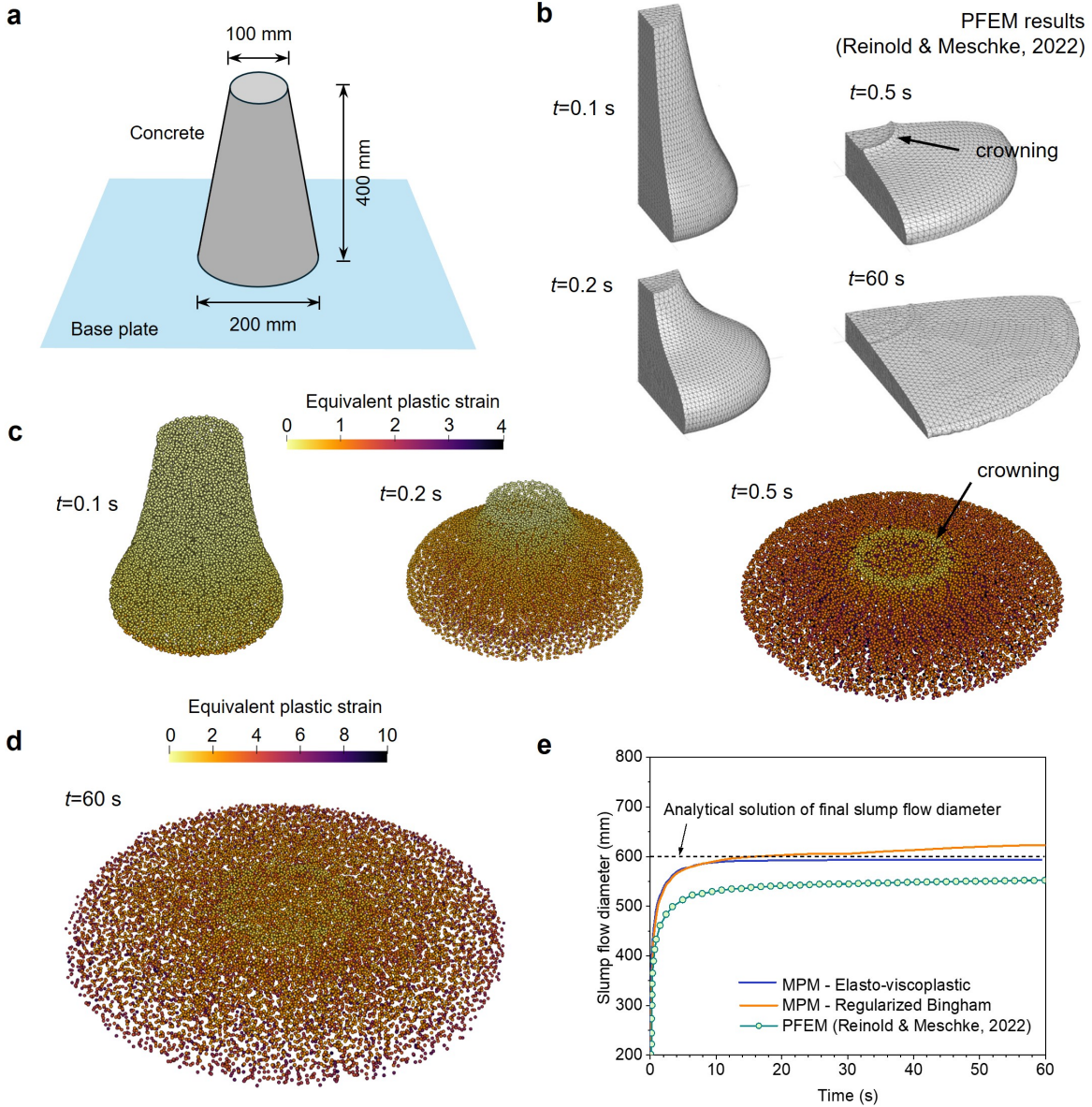


Figure 7: Roussel's slump flow benchmark (Roussel et al., 2016a): (a) Geometry of the concrete cone; (b) simulation results of the concrete slump flow by PFEM (Reinold and Meschke, 2022); (c) simulation results of the concrete slump flow at  $t = 0.1, 0.2$ , and  $0.6$  s; (d) final shape of the concrete flow ( $t = 60$  s); and (e) comparison of the evolution of the slump flow diameter using the elasto-viscoplastic solid model and the regularized Bingham fluid model. The crowning-like region highlighted in (b) and (c) shows the unsheared (plug) domain at the top tip of the concrete slump.

and our simulation results. This discrepancy may be attributed to numerical diffusion associated with the smoothing and projection of internal variables during re-meshing in their PFEM framework, as discussed by the authors themselves.

In Fig. 8, a more detailed comparison of the cross-section profile between the simulations and the analytical solution is provided. It can be observed that the MPM simulation using the elasto-viscoplastic model matches the analytical solution with good accuracy

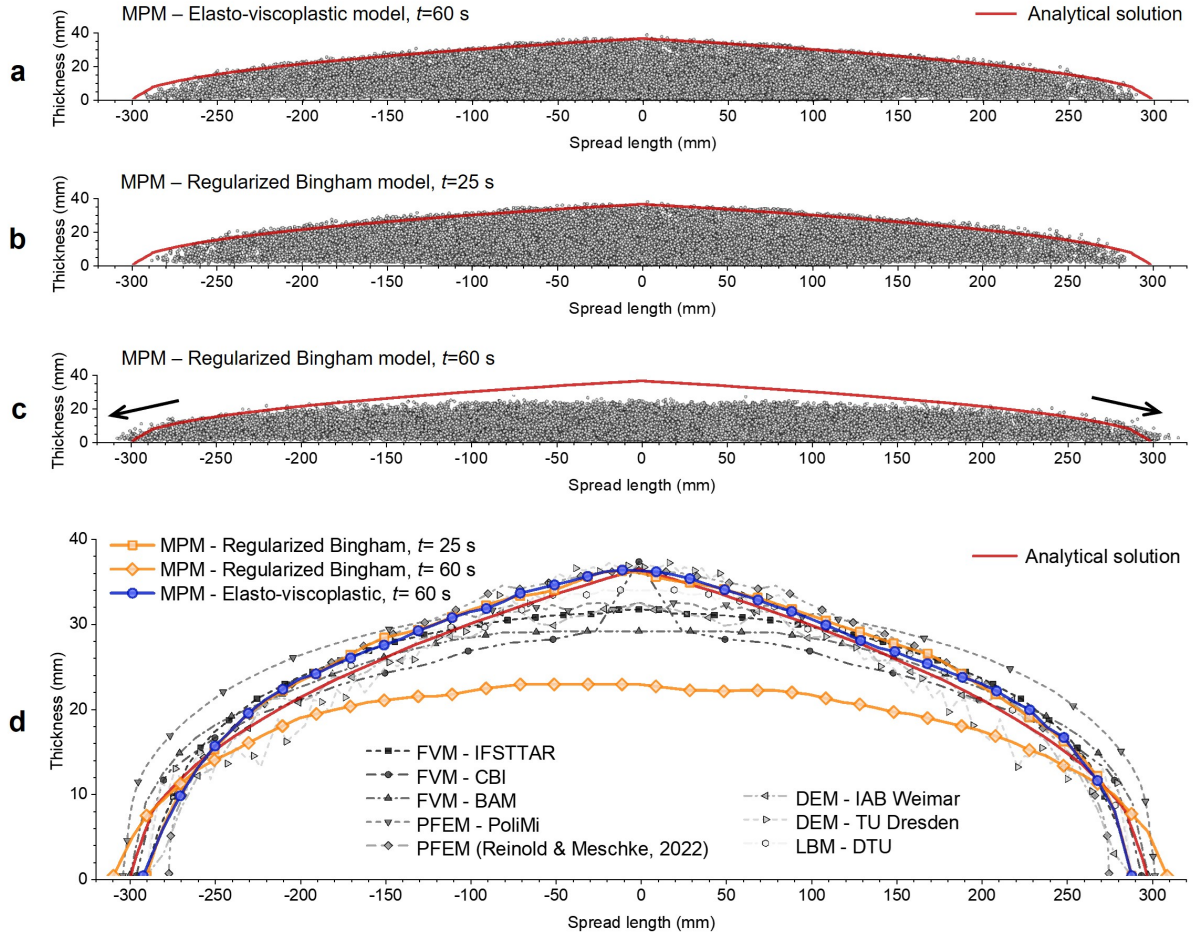


Figure 8: Roussel's slump flow benchmark (Roussel et al., 2016a): Comparison between MPM simulation results and analytical solution for surface profile: (a) elasto-viscoplastic model at  $t = 60$  s, (b) regularized Bingham model at  $t = 25$  s, and (c) regularized Bingham model at  $t = 60$  s. (d) Comparison of MPM simulation results with other numerical methods. Black arrows in (c) highlight that the concrete slump continues to flow outward even at  $t = 60$  s.

(Fig. 8a). The simulation using the regularized Bingham fluid model also shows good agreement at  $t = 25$  s (Fig. 8b). However, because the fluid model continues to flow to carry shear stress, the simulation at  $t = 60$  s exhibits noticeable deviation and an over-estimation of the spread (Fig. 8c). This spreading trend would continue if the simulation were extended further.

In Fig. 8d, results from various methods compiled by Roussel et al. (2016b) are compared. Although most of these methods are based on fluid models and provide reasonably good predictions, they often rely on artificial flow-stop criteria (for example, terminating the simulation at 20 s) (Roussel et al., 2016a; Wilkes et al., 2023), chosen solely for convenience and without physical justification. Such approaches, however, are unsuitable for long-duration simulations, including real-time casting scenarios. In contrast, the proposed elasto-viscoplastic model accurately captures the cessation of concrete flow and the final

spread without requiring any ad hoc stopping criteria.

#### 4.1.2. Validation of dynamic evolution of slump flow

In Roussel's benchmark test discussed in Section 4.1.1, the analytical solution is derived under quasi-static assumptions and therefore only provides the final surface profile, offering no means of validating the dynamic evolution of the flow. However, accurately capturing the transient flow behavior is crucial for simulating concrete casting processes. To evaluate the capability of our model in this regard, we consider and simulate a series of laboratory slump flow tests conducted by [Luo \(2014\)](#). In these laboratory tests, an Abrams cone is placed on a flat surface, filled with fresh concrete as illustrated in Fig. 9a, and then lifted vertically at a controlled speed to allow the material to flow outward in all directions. The entire flow process is recorded using high-speed cameras, and the measured SF distances are compared with the numerical simulations.

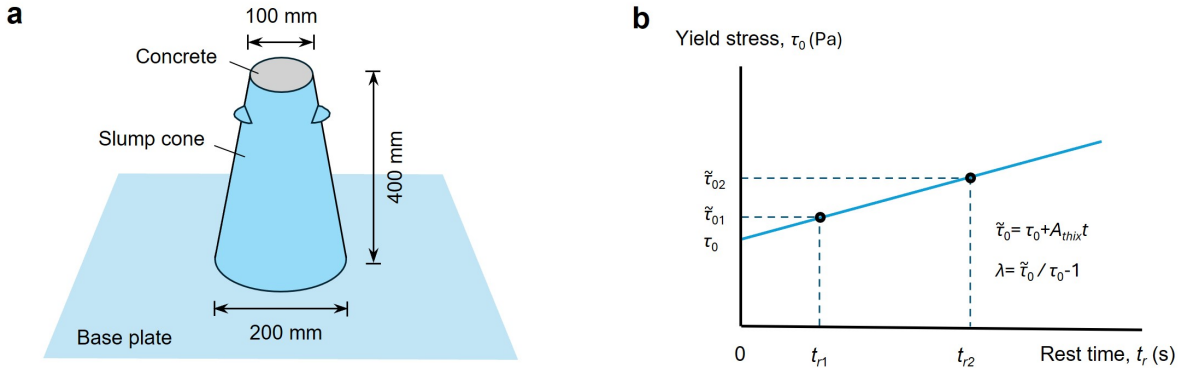


Figure 9: Dynamic evolution of slump flow: (a) Model setup of the concrete slump flow test in the experiment. (b) Linear fitting of the thixotropic parameters. Effective yield stresses  $\tilde{\tau}_{01}$  and  $\tilde{\tau}_{02}$  are measured at  $t_{r1}$  and  $t_{r2}$ , and  $\tau_0$ ,  $A_{thix}$ , and initial  $\lambda$  values are derived.

We selected four concrete slump flow tests as validation cases, as summarized in Table 1. These cases include two types of cement (i.e. CEM I and CEM II), two water-to-cement ratios (i.e. W/C = 0.5 and 1.0), and two bentonite contents (i.e. Bt = 4% and 8%). Generally, a higher water-to-cement ratio increases the flowability of concrete, while, in contrast, a higher bentonite content decreases it. For each concrete mix, slump flow tests are conducted at two rest times,  $t_r = 30$  and 120 s, denoted as SF30 and SF120, respectively. Based on the effective yield stress ( $\tilde{\tau}_0$ ) obtained from SF30 and SF120, the initial yield stress ( $\tau_0$ ) and the flocculation rate ( $A_{thix}$ ) are estimated through linear fitting (see Fig. 9b). For all the tests in this section, the deflocculation rate,  $\alpha$ , is set to a small value of 0.01 ([Wilkes et al., 2023](#)). The initial flocculation state variable  $\lambda$  can be determined accordingly. It is important to note that the plastic viscosity ( $\eta$ ) and the base plate friction coefficient ( $\mu_f$ ) need to be calibrated due to the lack of experimental data. Here,  $\mu_f$  is fixed at a value of 0.3, while  $\eta$  is calibrated. Furthermore, to accurately

Table 1: Dynamic evolution of slump flow: Summary of test conditions, material parameters, and measured slump flow diameter in experiments.

Concrete mix ID	Test	$t_r$ (s)	$\rho$ (kg/m <sup>3</sup> )	$\tilde{\tau}_0$ (Pa)	$\tau_0$ (Pa)	$A_{\text{thix}}$ (Pa/s)	$\lambda$ -	$\eta$ (Pa s)	$\mu_f$ -	$SF_{\text{exp}}$ (mm)
Mix-1	CEMI: WC0.5-Bt4%	SF30	30	1820	74.9	16.8	1.94	3.45	25*	529
		SF120	120		249.1			13.8		416
Mix-2	CEMII: WC0.5-Bt4%	SF30	30	1820	101.5	67.8	1.12	0.50	23*	497.5
		SF120	120		202.6			1.99		433
Mix-3	CEMII: WC1.0-Bt8%	SF30	30	1440	6.9	2.97	0.13	1.33	10*	810
		SF120	120		18.7			5.30		665
Mix-4	CEMII: WC0.5-Bt8%	SF30	30	1830	1000	900	-	-	50*	244
		SF120	120		1300					219

\* Calibrated value.

Note: WC - water-to-cement ratio; Bt - bentonite content; SF30/SF120 - slump flow with rest time of 30 s/120 s;  $t_r$  - rest time;  $\rho$  - density of concrete mix;  $\tilde{\tau}_0$  - effective yield stress at  $t_r > 0$ ;  $\tau_0$  - initial yield stress at  $t_r = 0$ ;  $A_{\text{thix}}$  - flocculation rate;  $\lambda$  - flocculation state variable;  $\eta$  - plastic viscosity;  $\mu_f$  - friction coefficient of base plate; and  $SF_{\text{exp}}$  - experimental slump flow diameter.

replicate the slump flow process observed in the laboratory, the bucket outside the concrete cone (mold) is modeled using rigid particles, and the lifting speed is controlled at 0.15 m/s. In addition, the elastic material parameters of the mixes are set as follows: Young's modulus  $E = 1 \times 10^5$  Pa and Poisson's ratio  $\nu = 0.45$  (Roussel et al., 2012a; Bolton and McKinley, 1997; Wilkes et al., 2023). A time step of  $\Delta t = 5 \times 10^{-4}$  s is used in the simulation.

Fig. 10a-d compares the obtained simulation results and experimental data for the four concrete mixes. From the simulation results, it is observed that for all cases, the slump flow diameter of SF120 is smaller than that of SF30. This result is expected, as the additional 90 seconds of rest time increases the yield stress of the SF120 case, thereby reducing its flowability. Furthermore, the evolution of the SF diameter initially increases slowly, likely due to the constraint imposed by the cone boundary, then accelerates, and finally decelerates, with all cases ceasing flow after approximately 0.4 s. This demonstrates the capability of the elasto-viscoplastic model to effectively capture the cessation of concrete flow. For Mix-1 and Mix-2 (see Fig. 10a and b), the simulated SF diameter evolution agrees well with experimental measurements, with final diameters in the range of 400–600 mm, which is typical for tremie concrete slump flow. This demonstrates that our model can not only accurately predict the final slump flow diameter but also capture the entire flow dynamics. In the case of Mix-3 and Mix-4 (see Fig. 10c and d), which exhibit significantly stronger and weaker flowability, respectively, the simulation shows slight deviations from experimental data; however, the overall trends remain consistent, and

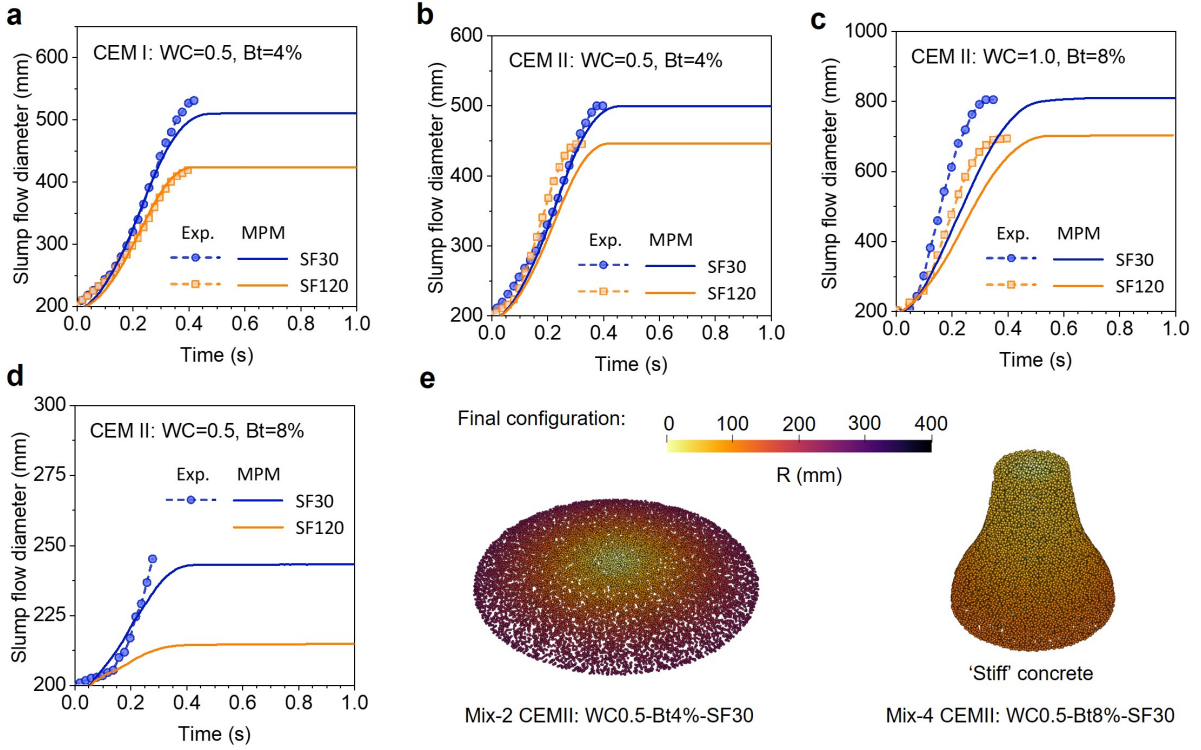


Figure 10: Dynamic evolution of slump flow: (a-d) Comparison of the dynamic evolution of slump flow diameter obtained by MPM simulation and laboratory test. (e) Final simulation snapshot from Mix-2 and 4.

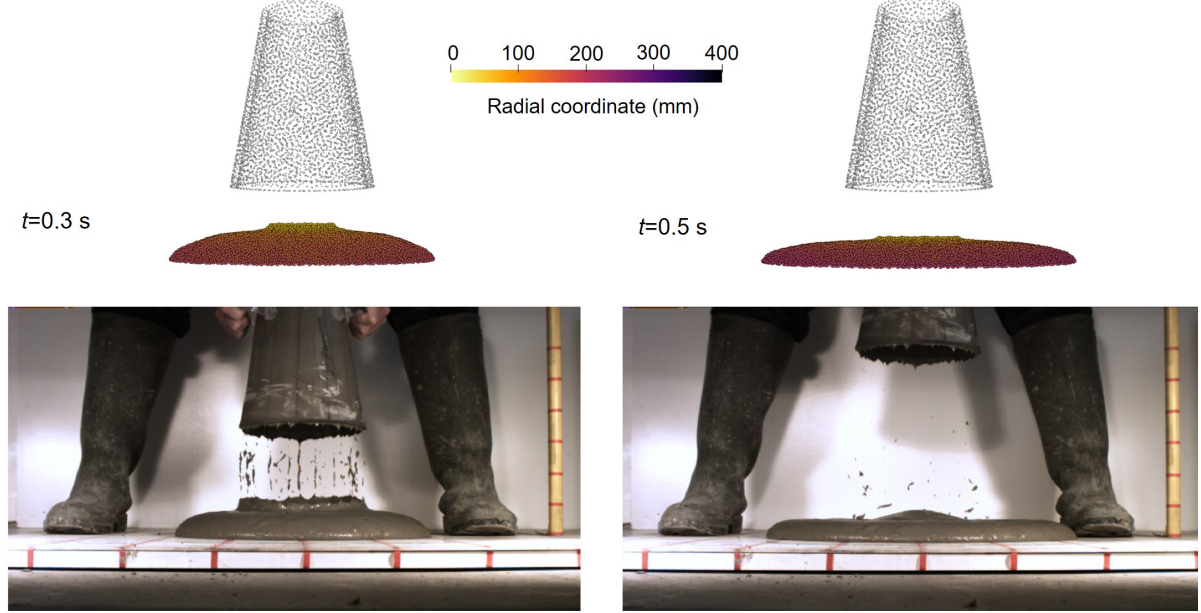
the discrepancies are within acceptable ranges.

Fig. 10e presents the final simulated profiles of a more workable concrete (Mix-1) and a less workable concrete (Mix-4), illustrating the model's ability to replicate the distinct flow behaviors associated with different levels of workability. Additionally, as shown in Figs. 11–12, comparisons between the simulated profiles and photographed experimental results for Mix-2-SF30, Mix-3-SF120, and Mix-4-SF30 further validate the model's accuracy across a range of concrete mixtures, from highly flowable to low-flowability compositions. These results demonstrate the versatility and robustness of the proposed modeling framework.

#### 4.1.3. Modeling the thixotropic behavior by slump flow tests

To demonstrate the capability of the developed elasto-viscoplastic model in simulating thixotropic concrete, the results of numerical simulations are compared against experimental slump flow tests performed on-site on production mixes. Yield stress, plastic viscosity, and slump flow (SF) values are obtained from an EFFC and DFI data set report of concrete tests performed on Tremie Concrete from numerous European and North American sites (Kränel, 2018; Feys and Khayat, 2018). Two typical concrete mixes from this data set, referred to as Mix-A and Mix-B, are chosen based on the range of concrete

**a Mix-2 CEMII: WC0.5-Bt4%-SF30**



**b Mix-3 CEMII: WC1.0-Bt8%-SF120**

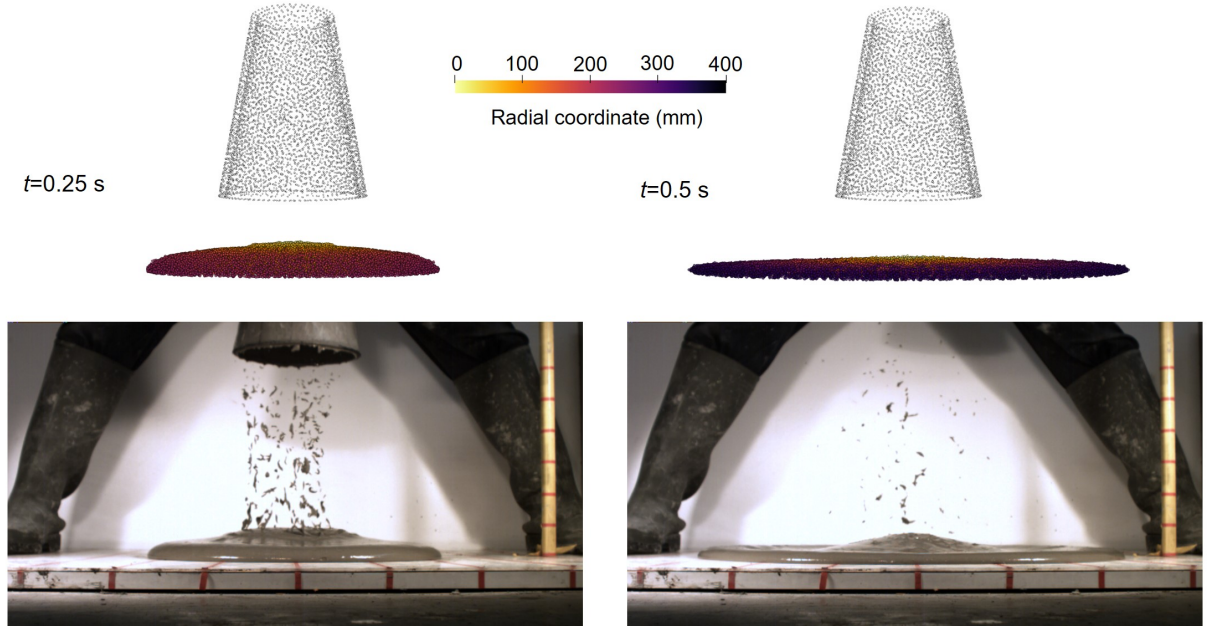


Figure 11: Dynamic evolution of slump flow: Comparison of the concrete slump profiles from MPM simulations and laboratory tests at  $t = 0.3$  s and  $t = 0.5$  s for (a) Mix-2 (CEMI: WC0.5-Bt4%-SF30) and (b) Mix-3 (CEMI: WC1.0-Bt8%-SF120). Experiment photos are taken from [Luo \(2014\)](#).

properties they represent. The flocculation parameter,  $A_{\text{thix}}$ , is determined by performing a linear regression from the effective yield stress data  $\tilde{\tau}_0$  measured at different rest times, as shown in Fig. 13. It is important to emphasize that this linear fit is used solely to derive  $A_{\text{thix}}$ . In our simulations, we still use the measured values of  $\tau_0$  rather than the

**Mix-4 CEMII: WC0.5-Bt4%-SF30**



Figure 12: Dynamic evolution of slump flow: Comparison of the concrete slump profiles from MPM simulation and laboratory test at  $t = 1.0$  s for Mix-4 (CEMII: WC0.5-Bt4%-SF30), a less workable concrete. Experiment photos are taken from [Luo \(2014\)](#).

fitted values (i.e. 92 and 139 Pa for Mix-A and Mix-B, respectively). The flocculation state  $\lambda$  can then be calculated from the measured yield stresses,  $\lambda = \tilde{\tau}_0/\tau_0 - 1$ . The final fitted  $A_{\text{thix}}$  are approximately 0.39 for Mix-A and 0.88 for Mix-B. According to Roussel's classification criteria ([Roussel, 2006b](#)), Mix-A and Mix-B fall under thixotropic concrete (with  $0.1 < A_{\text{thix}} < 0.5$ ) and highly thixotropic concrete (with  $A_{\text{thix}} > 0.5$ ), respectively. The report documents the slump flow diameter of Mix-A and Mix-B at rest time ( $t_r$ ) of 0s, 240s, and 600s, denoted as SF0, SF240, and SF600. Other model parameters for the two concrete mixes are shown in Table 2.

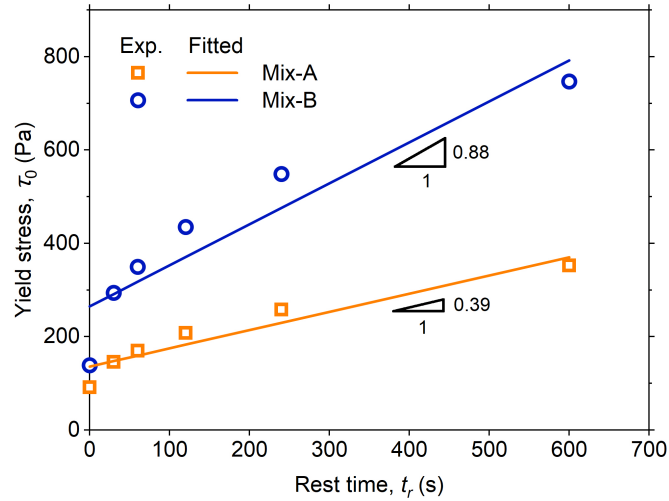


Figure 13: Thixotropic slump flow: Calculation of the flocculation parameter  $A_{\text{thix}}$  by linear regression of effective yield stress data.

It should be noted that the parameters  $\alpha$  and  $\mu_f$  are not provided in the EFFC/DFI report. Typically, these parameters are related to the properties of concrete and, therefore, require calibration. Considering that the value of  $\alpha$  has minimal impact on the simulation results for concrete immediately after mixing (i.e. Test SF0), we calibrated  $\mu_f$  using this experimental dataset and set  $\alpha = 0$  for this purpose. Then, by assuming that  $\mu_f$  is

a constant for the same concrete mix with different rest times. we calibrated  $\alpha$  using the experimental results for SF240 and SF600. Given the unavoidable errors in both experimental and simulation tests, we deemed a gap between SF<sub>mpm</sub> and SF<sub>exp</sub> within  $\pm 30$  mm to be acceptable. For Mix-A and Mix-B, the calibrated values of  $\mu_f$  are 0.30 and 0.35, respectively, both of which fall within a reasonable range for friction coefficients. The corresponding calibrated values of  $\alpha$  are 0.15 and 0.4. This trend suggests a positive correlation between the deflocculation rate  $\alpha$  and the flocculation rate  $A_{thix}$ . Such behavior is consistent with the established understanding of thixotropy in cementitious materials, in which structural build-up at rest and structural breakdown under shear arise from the same reversible flocculated microstructure. Experimental studies have shown that mixtures exhibiting stronger or faster flocculation tend to form larger but mechanically weaker flocs, which are more susceptible to shear-induced breakage, and that the extent of structural breakdown is closely linked to the subsequent capacity for structural rebuild (Roussel et al., 2012b; Ferron et al., 2013; Ye et al., 2024).

Table 2: Thixotropic slump flow: Summary of test conditions, material parameters, and measured slump flow diameter in experiments and MPM simulations.

Mix ID	Test	$t_r$ (s)	$\rho$ (kg/m <sup>3</sup> )	$\tilde{\tau}_0$ (Pa)	$\tau_0$ (Pa)	$A_{thix}$ (Pa/s)	$\lambda$ -	$\alpha$ -	$\eta$ (Pa s)	$\mu_f$ -	SF <sub>exp</sub> (mm)	SF <sub>mpm</sub> (mm)
Mix-A	SF0	0		92			0				535	532
	SF240	240	2400	258	92	0.39	1.8	0.15*	19.5	0.30*	500	493
	SF600	600		353			2.8				460	472
Mix-B	SF0	0		139			0				455	459
	SF240	240	2400	549	139	0.88	2.9	0.40*	29	0.35*	430	420
	SF600	600		747			4.4				420	395

\* Calibrated value.

Note: SF<sub>exp</sub> - experimental slump flow diameter; and SF<sub>mpm</sub> - simulated slump flow diameter by MPM using the elasto-viscoplastic model.

Fig. 14 compares the slump flow obtained from MPM simulations using the elasto-viscoplastic solid model and the PR-Bingham fluid model against experimental measurements. For the solid model, employing a unified set of parameters ( $\tau_0$ ,  $A_{thix}$ , and  $\alpha$ ) generally reproduces the physical test results across various thixotropic states (from SF0 to SF600). Specifically, for Mix-A, the simulated slump flow values closely align with experimental data (SF<sub>exp</sub>), with deviations within  $\pm 15$  mm. Additionally, the decrease in slump flow (i.e.  $\Delta SF$ ) at rest durations of 240 s and 600 s is also well captured: the experimental results are 35 mm and 75 mm, while the simulated values are 39 mm and 60 mm, respectively.

Despite its simplicity, the solid model effectively simulates the cessation of concrete flow, a critical behavior that the fluid model fails to capture. As illustrated in Fig. 14,

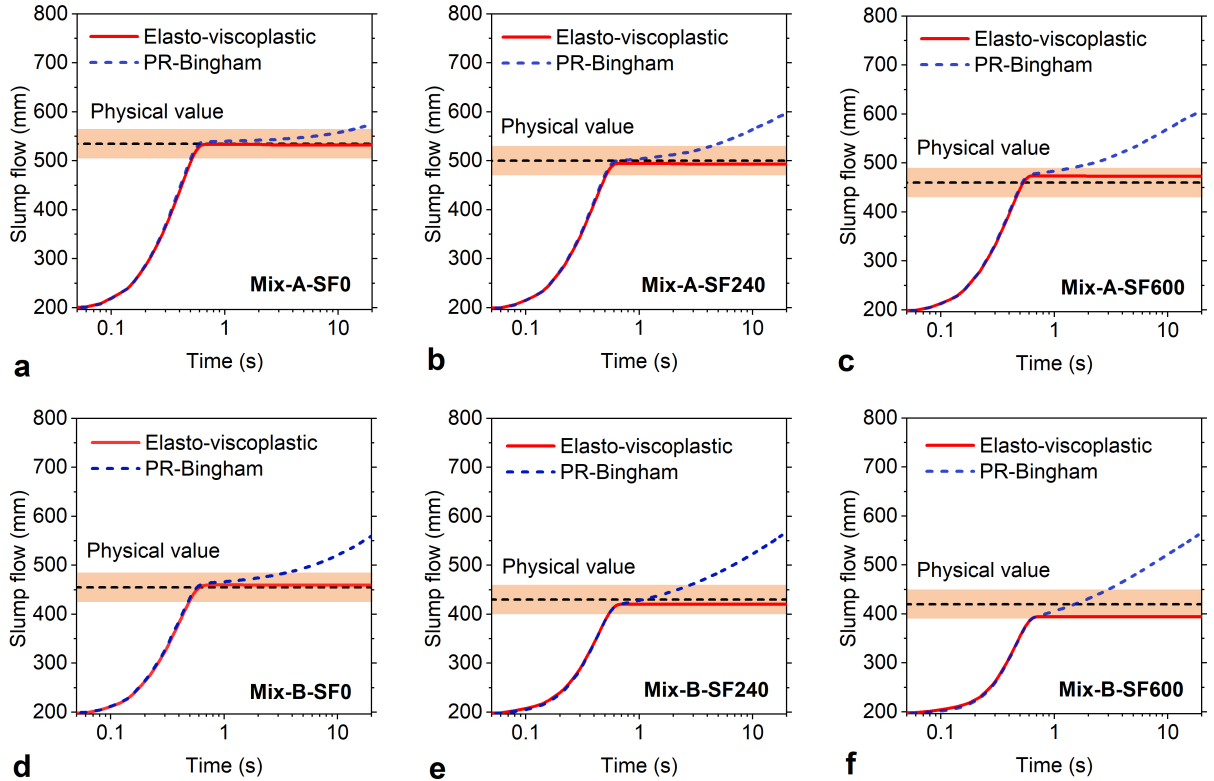


Figure 14: Thixotropic slump flow: Comparison of simulated slump flow and the reported physical value. (a-c) Mix-A and (d-f) Mix-B. The orange-colored rectangular region represents the range of the physical SF  $\pm 30$  mm.

while both models produce nearly identical results during the initial stage, the fluid model predicts continuous flow, resulting in a non-physical overestimation of SF distance at 20 s. Figs. 15a and b show contour plots of the flocculation state variable  $\lambda$  for Mix-A at 0.6 s and 20 s, for both models. The corresponding temporal evolutions of  $\lambda$  and the shear rate  $\dot{\gamma}$  or  $\dot{\gamma}^p$  are presented in Figs. 15c and d. These results indicate that, while both models behave similarly at 0.6 s, the fluid model sustains a small but non-zero shear rate, causing  $\lambda$  to decrease continuously, and flow to persist. In contrast, the solid model shows a drop in shear rate to zero, accompanied by an increase in  $\lambda$ , indicating flow cessation and a transition to flocculation. This highlights the clear advantage of the proposed elasto-viscoplastic solid model in simulating concrete flow behavior. For illustrative purposes, Fig. 16 and 17 depict the flow profiles of Mix-A and Mix-B at selected time instants.

#### 4.2. L-box test

The L-Box test (BSI, 2010) is another widely adopted experiment for evaluating the flowability and passing ability of fresh concrete (Nguyen et al., 2006). This test observes the flow behavior of concrete in confined spaces, particularly through reinforcing bars, to assess its workability. As shown in Fig. 18, the L-Box apparatus consists of a concrete reservoir (200 mm  $\times$  100 mm  $\times$  600 mm), a rebar grid (3  $\times$  12 mm  $\Phi$  rebars), and an end

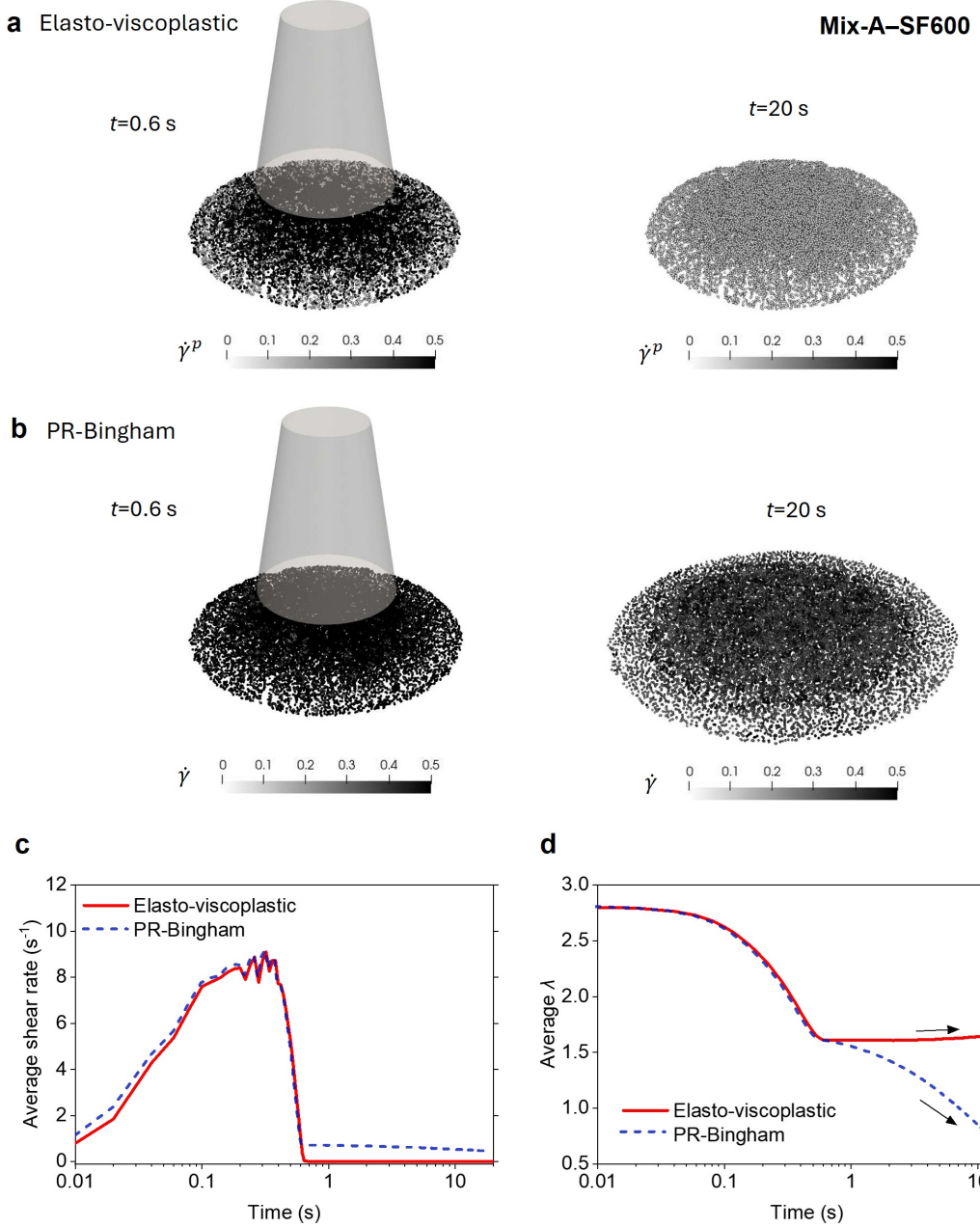


Figure 15: Thixotropic slump flow: Comparison of the simulation results of Mix-A-SF600 based on the elasto-viscoplastic solid model and the PR-Bingham fluid model. Contours of (a) plastic shear rate ( $\dot{\gamma}^p$ ) for elasto-viscoplastic model and (b) shear rate ( $\dot{\gamma}$ ) for PR-Bingham model at  $t = 0.6$  s and  $20$  s; and evolution of (c) average shear rate ( $\dot{\gamma}^p$  or  $\dot{\gamma}$ ) and (d) flocculation state variable  $\lambda$ . The arrows indicate opposite evolution trends of  $\lambda$  for the fluid and solid models as time progresses.

box ( $200$  mm  $\times$   $150$  mm  $\times$   $600$  mm). At the beginning of the test,  $12$  liters of concrete are poured into the reservoir and allowed to rest in an initial stationary state. Subsequently, the gate is opened, allowing the concrete to flow under gravity through the rebar grid and toward the end box.

Depending on the flow behavior of the concrete, the test results can be categorized

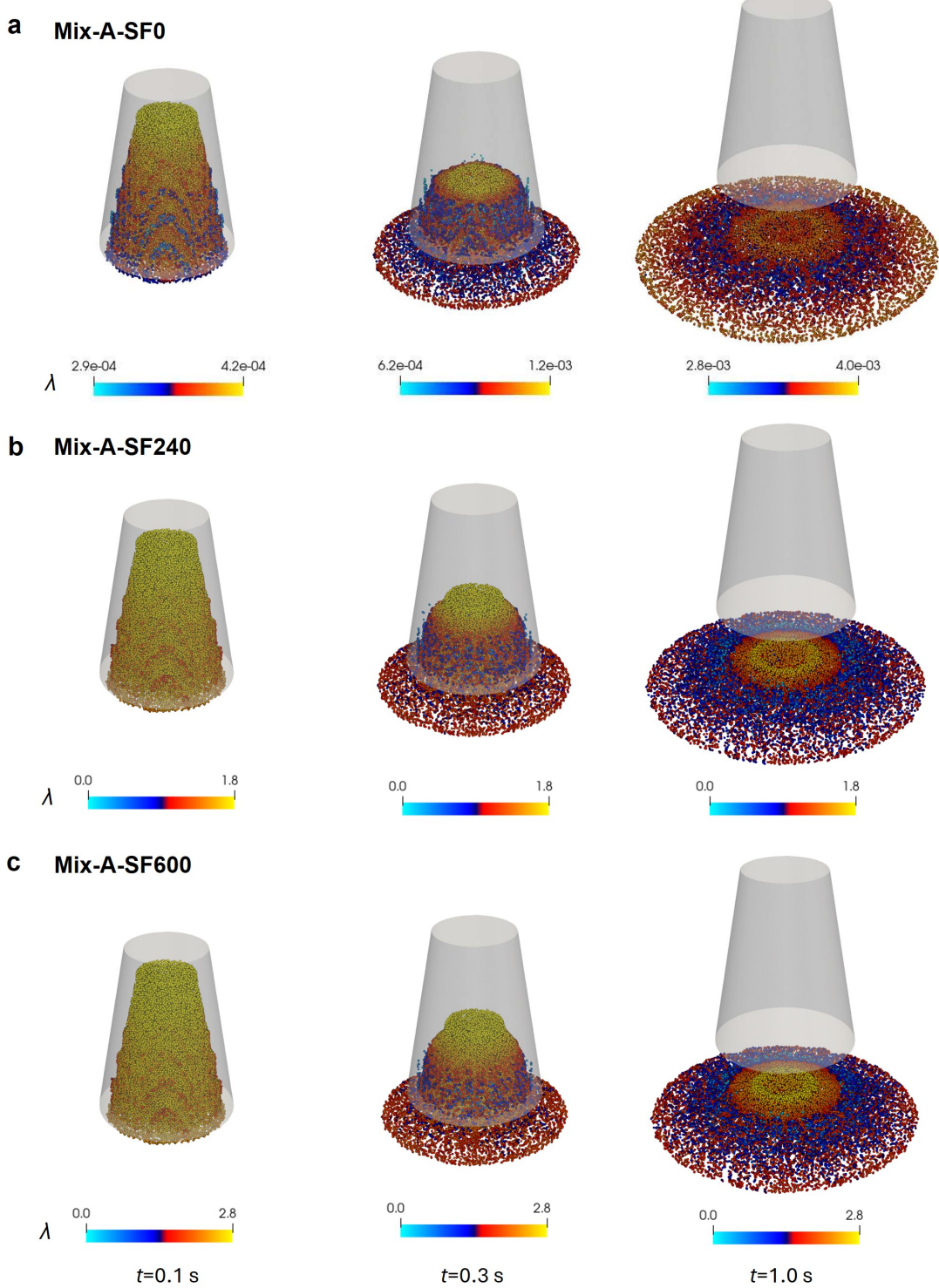
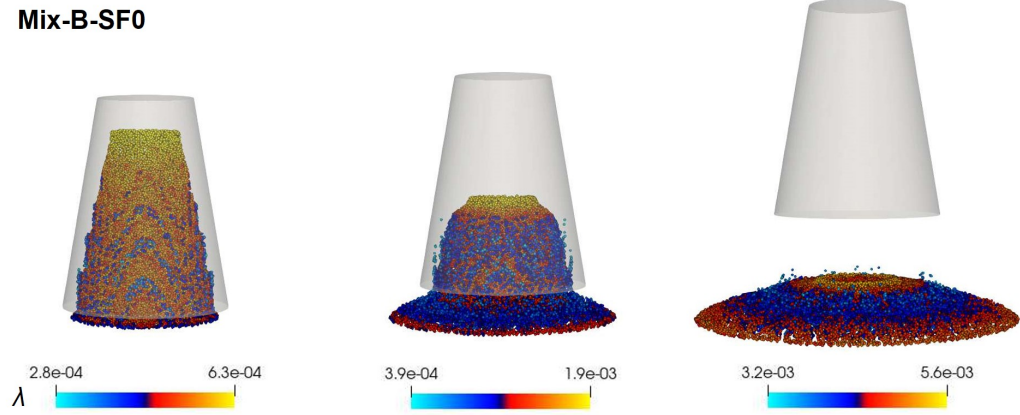


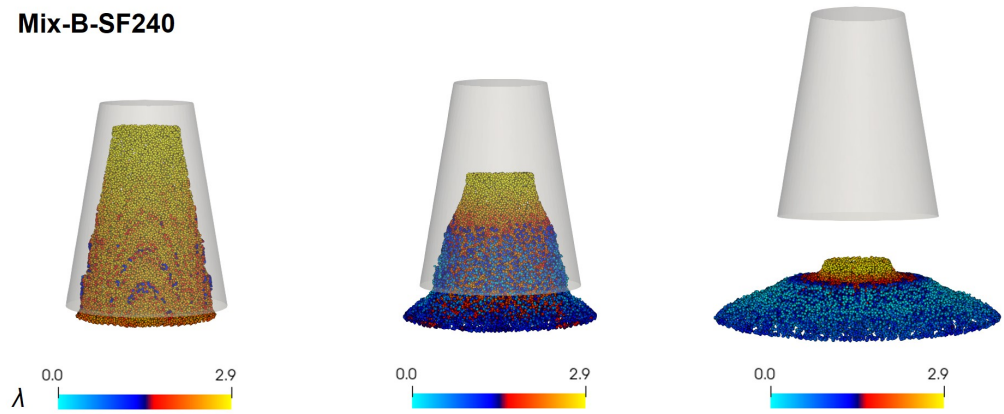
Figure 16: Thixotropic slump flow: Simulation results for Mix-A using the elasto-viscoplastic model at different time instants – (a) SF0, (b) SF240, and (c) SF600. The contours represent the values of the flocculation state variable  $\lambda$ .

into two typical cases:

**a Mix-B-SF0**



**b Mix-B-SF240**



**c Mix-B-SF600**

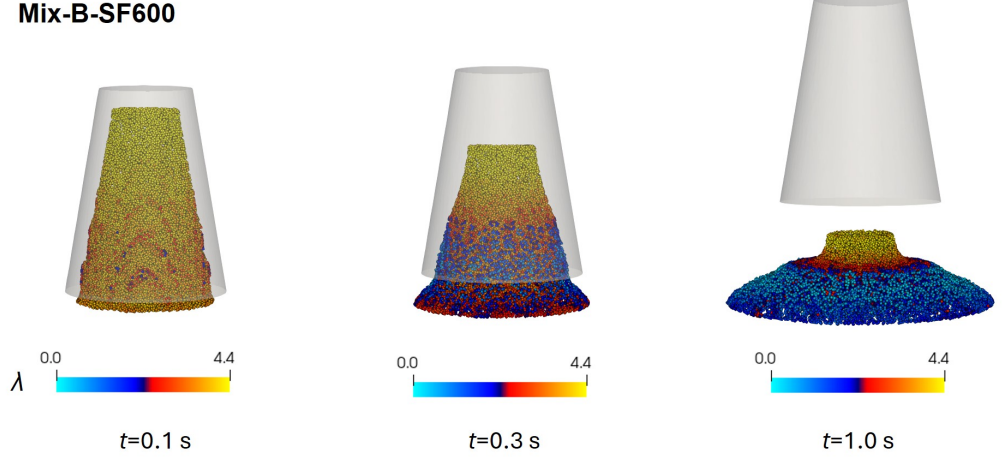


Figure 17: Thixotropic slump flow: Simulation results for Mix-B using the elasto-viscoplastic model at different time instants – (a) SF0, (b) SF240, and (c) SF600. The contours represent the values of the flocculation state variable  $\lambda$ .

1. Complete flow – concrete flow reaches the end of the end box. In this case, the time taken for the concrete to reach the end (denoted as  $t^{\text{end}}$ ) is recorded, along with the final height of the concrete at the end of the box after the flow has stopped (denoted as  $h$ ). The two parameters reflect the flow velocity and the passing ability of the concrete through the rebar grid.

2. Incomplete flow – concrete flow does not reach the end of the box due to excessive viscosity or insufficient flowability. In this scenario, the final flow distance of the concrete (denoted as  $d$ ) is measured, and the time at which the concrete ceases flow (denoted as  $t^{\text{final}}$ ) is also recorded to evaluate the extent of the flow and the location of the stagnation point.

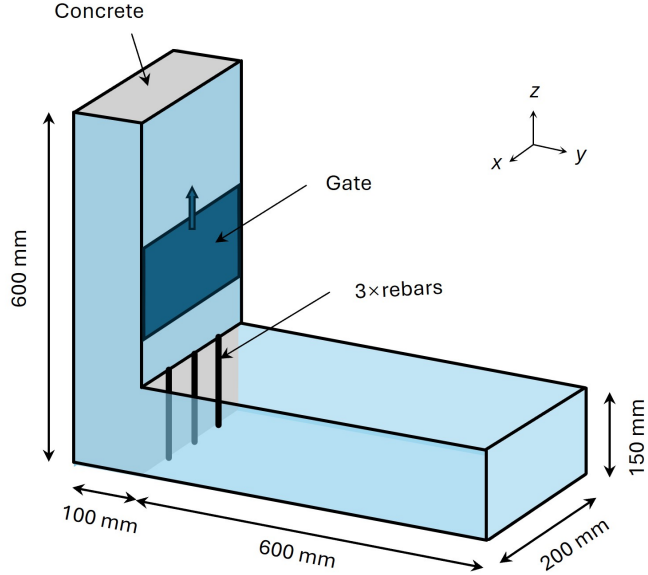


Figure 18: L-box test: Illustration of the geometry and model setup.

To simulate the L-box test, the entire computational domain is divided into uniform hexahedral grids. In the x-direction, three rebars are evenly placed, and the grid size is largely determined by the dimensions and positions of the rebars. Since accurately simulating the circular cross-section of the rebars is challenging, their cross-sections are simplified to rectangular shapes with a width equal to that of one grid cell. Considering that the rebars divide the L-box into four equal parts along the x-direction, 19 cells are created along this direction, each with a width of 10.5 mm. In the y- and z-directions, a uniform grid size of 10 mm is used. As a result, the dimensions of each grid cell are  $10.5 \times 10 \times 10$  mm. Due to the irregularity of the side length, isoparametric elements are considered. Each grid cell contains 8 material points, resulting in a total of 91,200 material points, ensuring high resolution and computational accuracy. The quasi-static stress under the self-weight of the concrete is adopted as the initial stress condition. Additionally, for computational simplicity, the gate opening time is assumed to be negligible, and thus, the gate-opening process is not explicitly simulated. Similarly, we simulate the flow behavior of two concrete mixes, Mix-A and Mix-B, at two different rest times ( $t_r = 0$  s and 600 s).

The experimental data, recorded from the EFFC and DFI datasets (Kränel, 2018; Feys and Khayat, 2018), served as a reference for validating the numerical model. The experimental results indicate that Mix-A is a complete flow, whereas Mix-B is an incomplete

Table 3: L-box test: Summary of test conditions, material parameters, and experimental/simulation results.

Mix ID	Test	$t_r$ (s)	$\tau_0$ (Pa)	$A_{thix}$ (Pa/s)	$\lambda$ -	$\alpha$ -	$\eta$ (Pa s)	$\mu_f$ -	$h_{exp}$ (mm)	$h_{mpm}$ (mm)	$t_{exp}^{\text{end}}$ (s)	$t_{mpm}^{\text{end}}$ (s)	
Mix-A	SF0	0	92	0.39	0	2.8	0.15 <sup>†</sup>	19.5	0.25*	70	50	1.4	1.1
	SF600	600			2.8				45	31	2.6	2.5	
Mix ID	Test	$t_r$ (s)	$\tau_0$ (Pa)	$A_{thix}$ (Pa/s)	$\lambda$ -	$\alpha$ -	$\eta$ (Pa s)	$\mu_f$ -	$d_{exp}$ (mm)	$d_{mpm}$ (mm)	$t_{exp}^{\text{final}}$ (s)	$t_{mpm}^{\text{final}}$ (s)	
Mix-B	SF0	0	139	0.88	0	4.4	0.40 <sup>†</sup>	29	0.45*	580	590	11.5	9
	SF600	600			4.4				520	520	13	10	

\* Calibrated value.

†  $\alpha$  is taken as the value calibrated from the slump flow test in Section 4.1.3.

Note:  $h$  and  $t^{\text{end}}$  are the height of the concrete at the end of the box and the time at which the concrete reaches the end, respectively;  $d$  and  $t^{\text{final}}$  denote the final flow distance and the time the concrete ceases to flow, respectively; and  $\square_{\text{exp}}$  and  $\square_{\text{mpm}}$  denote the experimental and simulated results using the elasto-viscoplastic model, respectively.

flow, representing two distinct flow behaviors. The material parameters and key experimental results are presented in Table 3 for reference. It should be noted that, since the same concrete mix as in the slump flow test is used, the previously calibrated deflocculation parameter  $\alpha$  is adopted for consistency (they are not recalibrated for this geometry). However, the friction coefficient  $\mu_f$ , being a property related to the interaction between the concrete and the contact interface, should be recalibrated. Similar to the slump flow test, we use the test  $t_r = 0$  to calibrate  $\mu_f$ . Here, we assume the friction coefficient for all boundary walls is the same. Finally, the calibrated  $\mu_f$  is 0.25 and 0.45 for Mix-A and Mix-B, respectively (see Table 3). Table 3 also presents key metrics measured in both the experiments and simulations, including  $t^{\text{end}}$  and  $h$  for Mix-A, as well as  $t^{\text{final}}$  and  $h$  for Mix-B. It can be observed that the  $\alpha$  values calibrated using the slump flow tests can also be successfully applied to the L-box simulations, yielding results that align well with the experimental data.

In this study, both Mix-A and Mix-B are simulated using the PR-Bingham fluid model using the same parameters, and the results are compared with those obtained from the elasto-viscoplastic solid model. Figs. 19a and b compare the evolution of the filling height of concrete at the end of the L-box for Mix-A with rest times of 0 s and 240 s, respectively. In both tests, the elasto-viscoplastic solid model and the PR-Bingham fluid model reached the end of the box at approximately the same time. However, the solid model ceased flowing after just 2 seconds, while the fluid model continued flowing for up to 40 seconds. Although the fluid model results in Fig. 19a appear to align more closely with the experimental data after the initial stage, this behavior is unphysical. In Fig. 19b, the

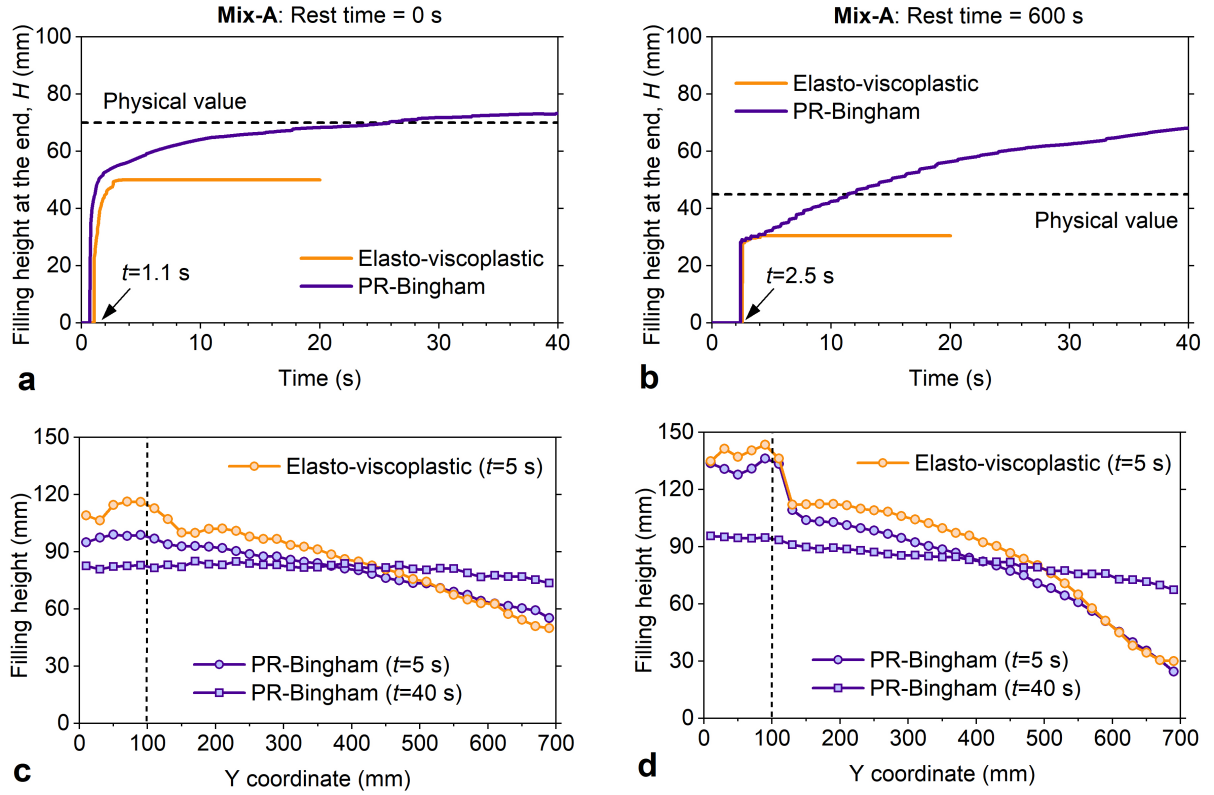


Figure 19: L-box test: Simulation results of Mix-A: (a-b) filling height at the end of the box; (c-d) surface configuration (along the central y-z plane) at different time instants. The left and right columns represent the results for rest times  $t_r = 0$  and  $t_r = 240$  s, respectively. The vertical dashed lines show where the L-box transitions from the concrete reservoir to the end box.

fluid model's results at 40 seconds significantly exceed the experimental values, and it is evident that this discrepancy would continue to increase if the simulation were extended further. Figs. 19c and d compare the free surface configurations of Mix-A at the end of the simulations. For the solid model, despite being simulated for only 20 seconds, the flow had completely stopped, resulting in a distinct sloped free surface. In contrast, the fluid model, even after 40 seconds, produced a nearly flat free surface.

A similar pattern is observed for Mix-B. Since Mix-B did not reach the end of the box before stopping flowing, Figs. 20a and b compare the flow distance instead. In the early stages of flow, the solid model and fluid model produced nearly identical flow fronts. However, the solid model stopped flowing after reaching distances of 590 mm and 520 mm for the respective tests, which matched the experimental results very well. Conversely, the fluid model continued flowing and eventually reached the end of the box, which is inconsistent with the experimental observations. Examining the final concrete shapes in Figs. 20c and d, the fluid model produced a nearly horizontal surface at 40 seconds. The inability to maintain the concrete's shape introduces significant distortions in the simulation results, with the degree of inaccuracy increasing as the simulation progresses.

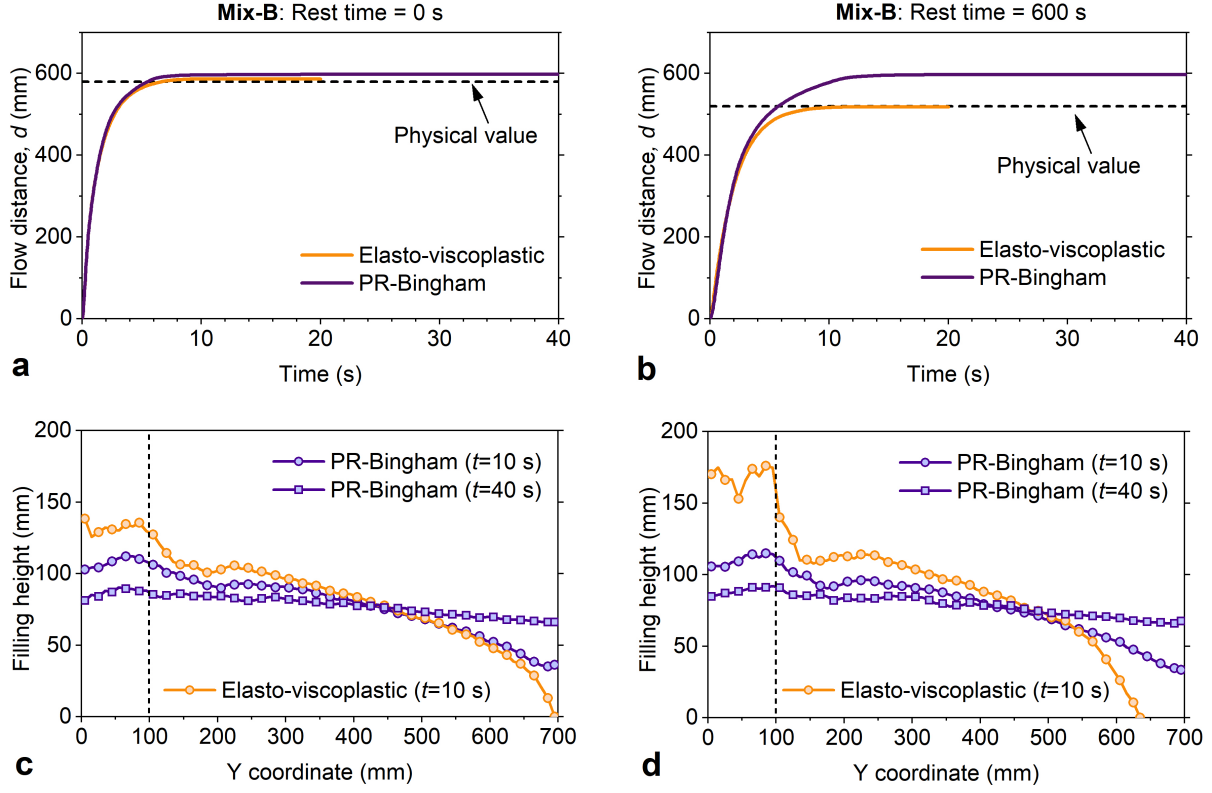


Figure 20: L-box test: Simulation results of Mix-B: (a-b) flow distance  $d$  measured from the transition between the concrete reservoir and the end box; (c-d) surface configuration (along the central  $y$ - $z$  plane) at different time instants. The left and right columns represent the results for rest times  $t_r = 0$  and  $t_r = 600$  s, respectively. The vertical dashed lines show where the L-box transitions from the concrete reservoir to the end box.

Figs. 21a-d and 22a-d illustrate the final concrete configurations for Mix-A and Mix-B, respectively, as simulated using the solid model and the fluid model. Meanwhile, Figs. 21e-f and 22e-f further compare the evolution of the average flocculation state parameter,  $\lambda$ , for both models. For cases with  $t_r = 0$ , both models exhibit a gradual increase in  $\lambda$  over time as flocculation process dominates. However, the  $\lambda$  of the fluid model increases at a slower rate compared to the solid model as time progresses, as the deflocculation rate term does not vanish as the fluid model keeps shearing over time. In contrast, for the solid model, the deflocculation rate term diminishes entirely, allowing for a more consistent accumulation of  $\lambda$ . For the case with  $t_r = 240$ , the initial values of  $\lambda$  for both the solid and fluid models are nearly identical. However, the fluid model continues to deflocculate throughout the simulation due to the same reason. Meanwhile, the solid model initially defloculates and exhibits further flocculation after the flow stops.

Finally, it is important to discuss the role of rebars. The L-box test is designed to simulate the ability of concrete to flow through narrow passages, such as the gaps between rebars. As concrete flows through the rebar grid, it experiences additional shearing,

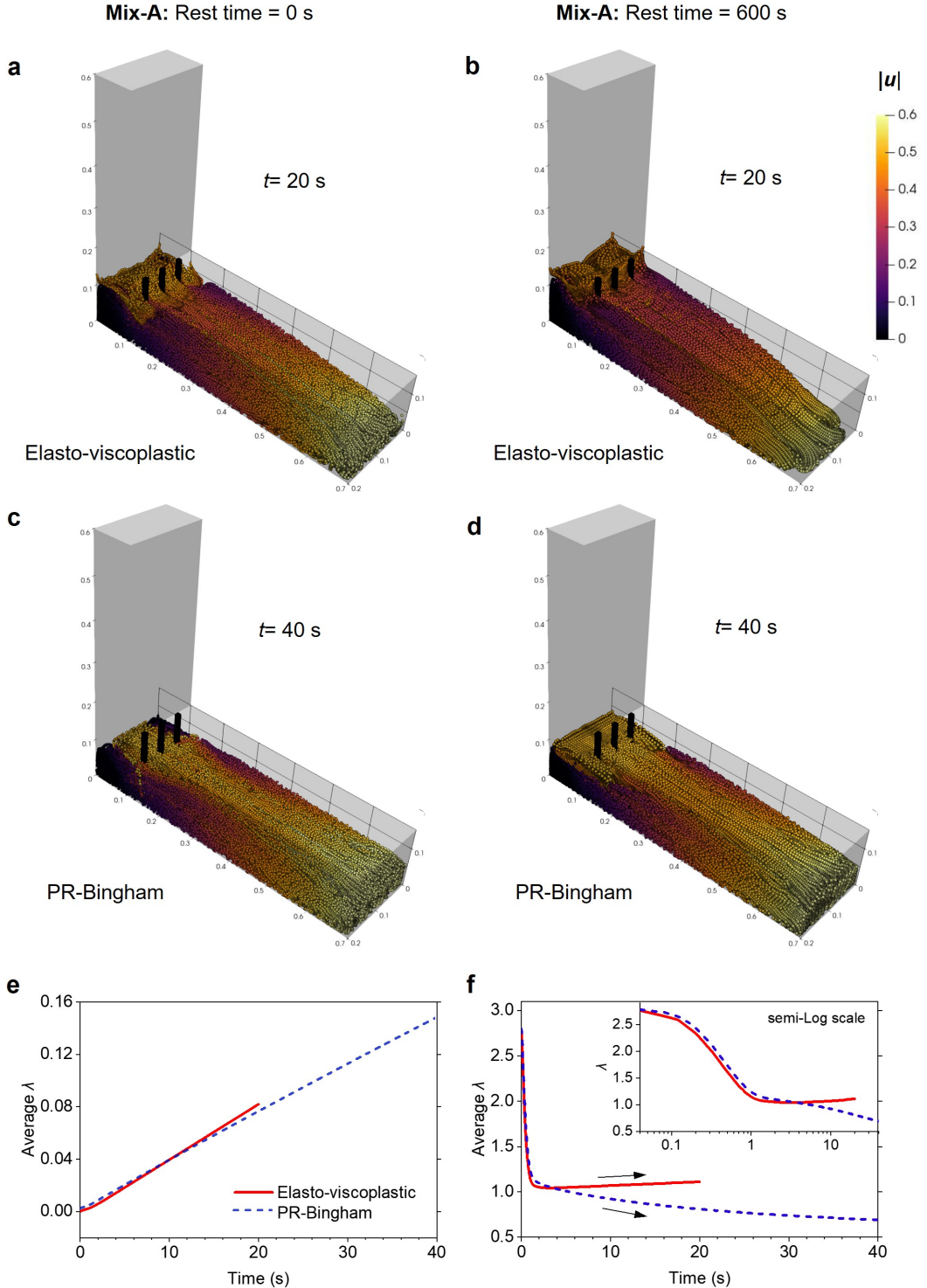


Figure 21: L-box test: Simulation results of Mix-A. (a-b) final concrete configuration simulated by the elasto-viscoplastic solid model; (c-d) final concrete configuration simulated by the PR-Bingham fluid model; (e-f) evolution of the flocculation state  $\lambda$  (calculated as the average value across all material points). The left and right columns represent the results for rest times  $t_r = 0$  and  $t_r = 240$  s, respectively. The arrows show opposite evolution trends of  $\lambda$  of the fluid and solid models as time progresses.

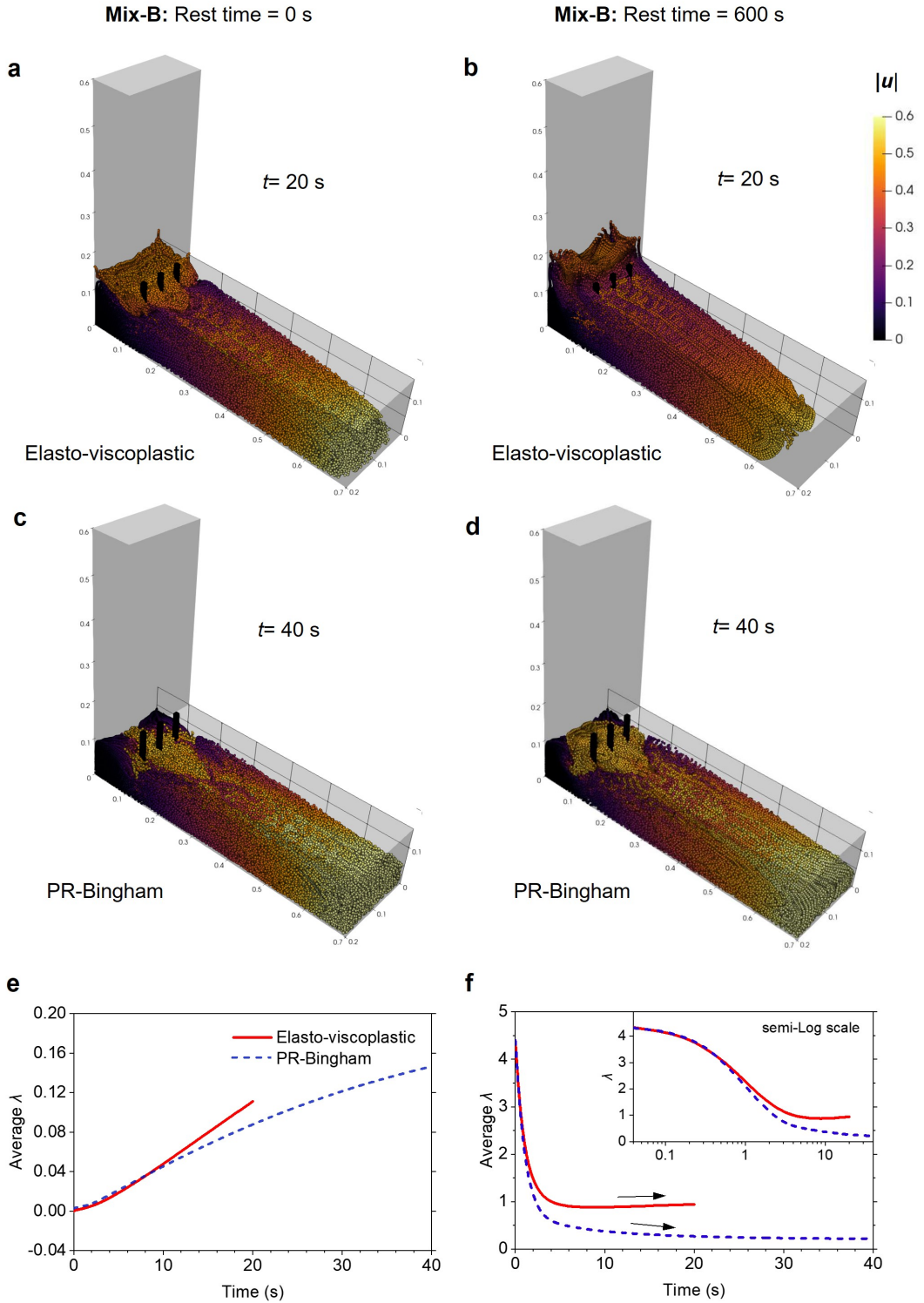
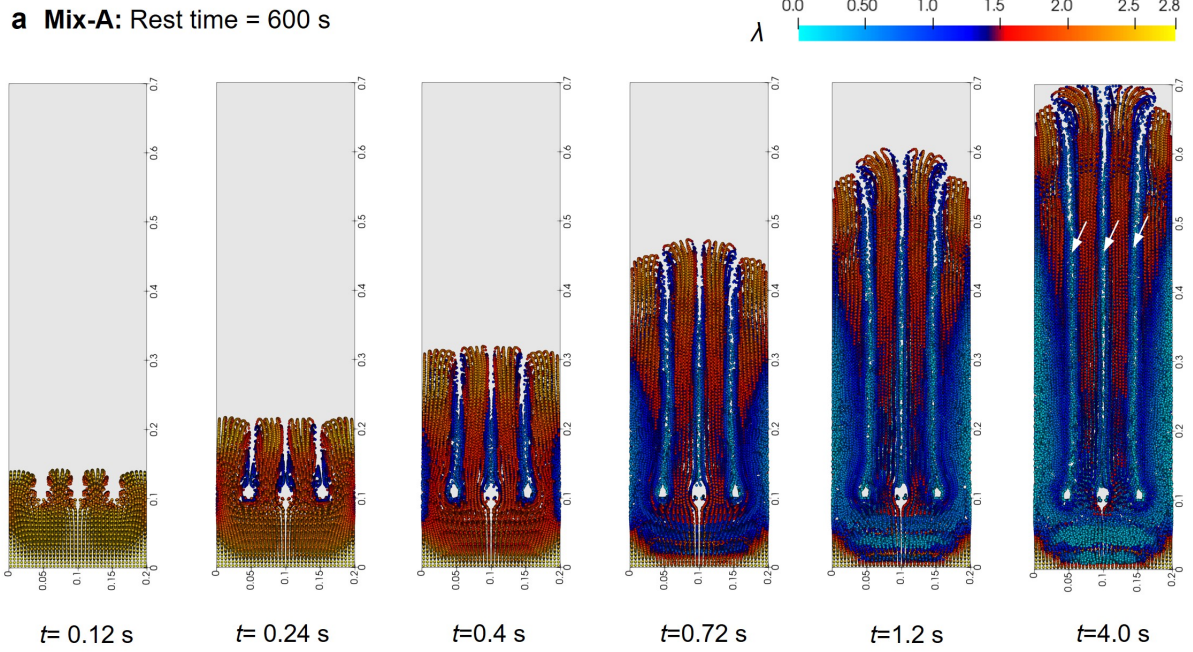


Figure 22: L-box test: Simulation results of Mix-B: (a-b) final concrete configuration simulated by the elasto-viscoplastic solid model; (c-d) final concrete configuration simulated by the PR-Bingham fluid model; (e-f) evolution of the flocculation state  $\lambda$  (calculated as the average value across all material points). The left and right columns represent the results for rest times  $t_r = 0$  and  $t_r = 240\text{ s}$ , respectively. The arrows show opposite evolution trends of  $\lambda$  of the fluid and solid models as time progresses.

**a Mix-A: Rest time = 600 s**



**b Mix-B: Rest time = 600 s**

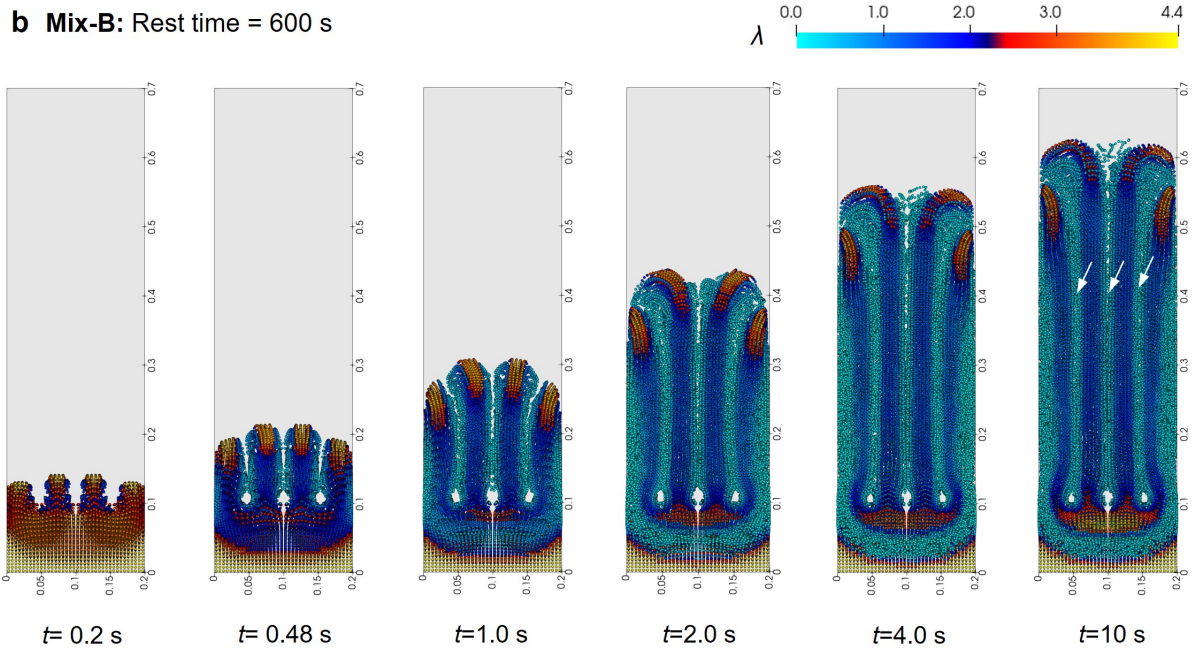


Figure 23: L-box test: Simulation results of the  $\lambda$  distribution at the cross-section  $z = 0.05$  m: (a) Mix-A at  $t = 0.12, 0.24, 0.4, 0.72, 1.2$ , and  $4.0$  s, and (b) Mix-B at  $t = 0.2, 0.48, 1.0, 2.0, 4.0$ , and  $10$  s. The white arrows highlight the three distinct low- $\lambda$  streaks due to the presence of rebars.

leading to rapid deflocculation. To observe this phenomenon, we extracted the  $\lambda$  profile at  $z = 0.05$ -m cross section at different time steps. Figs. 23a and b show the results for Mix-A and Mix-B, respectively. These figures illustrate the process of concrete being squeezed through the gaps between the rebars and gradually merging downstream. It

can be observed that the  $\lambda$  values of the concrete flowing near the sides of the rebars are significantly lower than those farther away from the rebars. As the concrete flows forward, three distinct low- $\lambda$  streaks emerge. This finding highlights the significant role of rebars in altering the flow pattern and flocculation state of the concrete. It also underscores the excellent performance of the proposed model in capturing the complex interactions between concrete and boundaries.

#### 4.3. *V-funnel test*

The V-funnel test (BSI, 2010) is a standard method used to evaluate the viscosity and filling ability of fresh concrete (Mu et al., 2022; Thanh et al., 2020; Alyhya et al., 2017). It measures the time required for a specific volume of concrete to flow through a narrow, funnel-shaped outlet under the influence of gravity. This test provides critical insights into the rheological properties of the concrete, such as its ability to flow smoothly without external compaction and resistance to segregation.

The standard geometry of the V-funnel, as illustrated in Fig. 24, consists of an inclined funnel-shaped container with a height of approximately 600 mm, a top opening of 515 mm  $\times$  75 mm, and a rectangular outlet at the bottom measuring 65 mm  $\times$  75 mm. The total volume of the funnel is about 12 liters. In the standard lab test procedure, the funnel is first filled with concrete, which is then left to rest for  $10 \pm 2$  seconds to allow air bubbles to escape and stabilize. The bottom gate is then opened, and the time from gate opening until the interior of the funnel becomes fully visible through the outlet is recorded. This time is defined as the V-funnel flow time ( $t_v$ ). If the concrete flow is discontinuous or blockage occurs, it indicates that the concrete's viscosity is too high, rendering it unsuitable for this test.  $t_v$  indirectly characterizes the viscosity and flowability of the concrete. A shorter  $t_v$  indicates better flowability, while an excessively long or discontinuous flow suggests high viscosity or insufficient flowability.

In the MPM simulation, a regular hexahedral grid is utilized as the background mesh, with a grid size of 10.72 mm. Frictional boundary conditions are applied to all walls, while step boundaries are used to discretize the inclined surfaces. The time step size is set to  $5 \times 10^{-5}$  s. Simulations are performed for both Mix-A and Mix-B; however, due to the absence of relevant experimental data, validation is not conducted. We continue to use the previously calibrated parameters, except for the friction coefficient, which is fixed at 0.3 for both Mix-A and Mix-B. Both the solid and fluid models are evaluated in the simulations. The measured  $t_v$  values for both solid and fluid models are summarized in Table 4. Additionally, Fig. 25 illustrates the evolution of the percentage of concrete volume passing through the bottom gate of the V-funnel for Mix-A and Mix-B at various rest times.

It can be observed that  $t_v$  increases slightly with rest time. This indicates that, in addition to depending on the plastic viscosity  $\eta$ ,  $t_v$  is also influenced by the yield stress

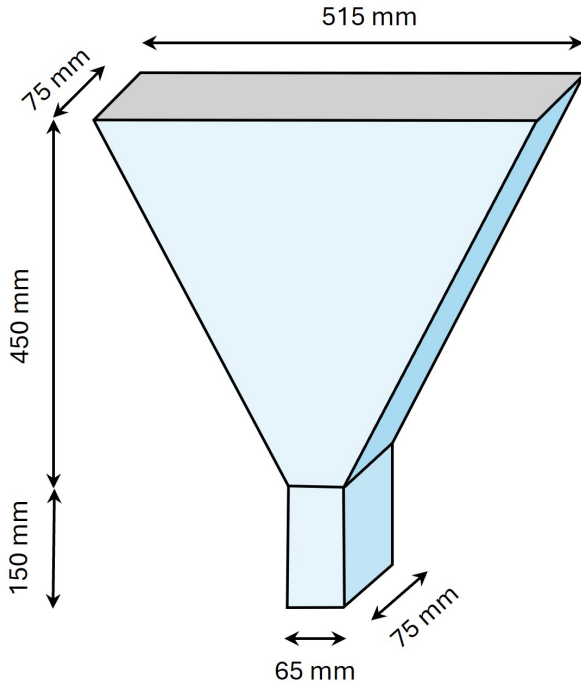


Figure 24: V-funnel test: Illustration of the geometry and model setup.

Table 4: V-funnel test: Summary of test conditions, material parameters, and simulation results.

Mix ID	Test	$t_r$ (s)	$\tau_0$ (Pa)	$A_{\text{thix}}$ (Pa/s)	$\lambda$ -	$\alpha$ -	$\eta$ (Pa s)	$\mu_f$ -	$t_{v, \text{solid}}$ (s)	$t_{v, \text{fluid}}$ (s)
Mix-A	SF0	0			0				1.40	1.36
	SF240	240	92	0.39	1.8	0.15 <sup>†</sup>	19.5	0.3	1.50	1.46
	SF600	600			2.8				1.54	1.50
Mix-B	SF0	0			0				1.68	1.66
	SF240	240	139	0.88	2.9	0.40 <sup>†</sup>	29	0.3	1.84	1.78
	SF600	600			4.4				2.00	1.84

<sup>†</sup>  $\alpha$  is taken as the value calibrated from the slump flow test in Section 4.1.3.

Note:  $t_{v, \text{solid}}$  and  $t_{v, \text{fluid}}$  denote the simulated V-funnel flow time using the elasto-viscoplastic solid model and the PR-Bingham fluid model, respectively.

through its effect on the apparent viscosity  $\eta_a$ . Comparing Mix-A and Mix-B shows that Mix-B, which has a higher plastic viscosity, consistently exhibits a larger  $t_v$ . The PR-Bingham model predicts slightly lower  $t_v$  values than the proposed elasto-viscoplastic model, and this difference grows with rest time, reaching a maximum of 1.6 seconds in the Mix-B-SF600 case. Nevertheless, the overall discrepancy between the two models remains small because, in the flowing regime, the elasto-viscoplastic model produces a velocity profile comparable to the PR-Bingham model, as verified in Section 3.3.

Figs. 26 and 27 further compare the thixotropy state parameter  $\lambda$  from both models

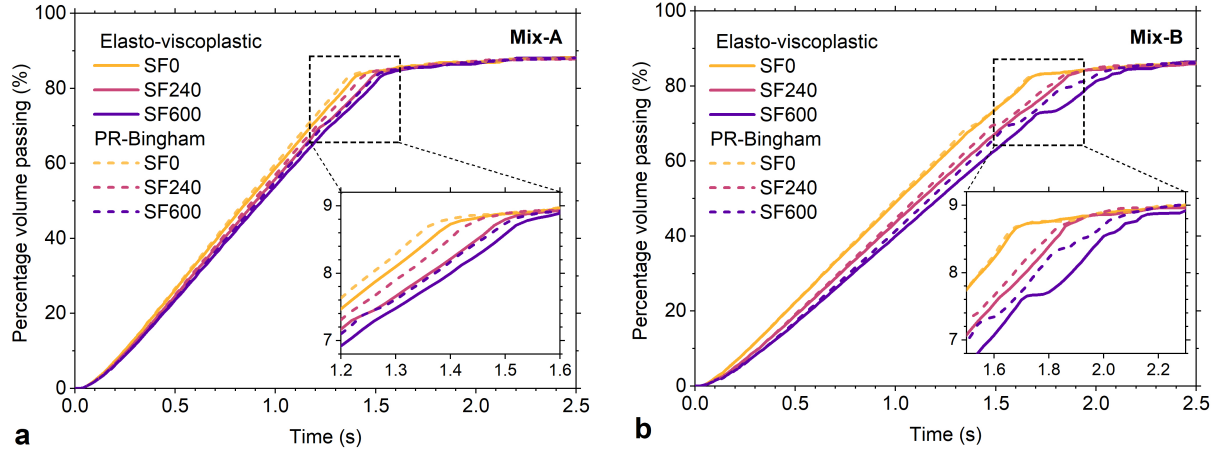


Figure 25: V-funnel test: Evolution of the percentage of concrete volume passing through the bottom gate of the V-funnel for (a) Mix-A and (b) Mix-B at various rest times.

and show that their predictions remain close throughout the V-funnel test. These results suggest that, for simulating the flow phase of concrete, the proposed elasto-viscoplastic solid model performs equivalently to the PR-Bingham fluid model. However, unlike the latter, the elasto-viscoplastic model also accurately captures the cessation of flow, providing a more physically realistic representation of the complete flow–rest transition behavior.

## 5. Conclusions and outlooks

This study developed a novel elasto-viscoplastic thixotropic model for simulating the flow and cessation behavior of fresh concrete. The model was implemented within the Material Point Method (MPM) framework to effectively handle large deformation flows. The key findings of this study can be summarized as follows:

- Unlike conventional fluid-based models such as the Bingham model, which rely on ad hoc stopping criteria, the proposed model treats fresh concrete as a rate-dependent elasto-viscoplastic solid within the continuum mechanics framework. This approach naturally captures flow cessation as stresses fall below the yield threshold, enabling a physically realistic transition to a static state.
- The integration of Roussel’s thixotropy model allows the simulation of flocculation-induced structural build-up during rest and shear-induced deflocculation during flow.
- An accurate stress integration algorithm based on the return-mapping concept was developed and implemented within the MPM framework, ensuring robust and consistent stress updates across flowing and resting regimes.

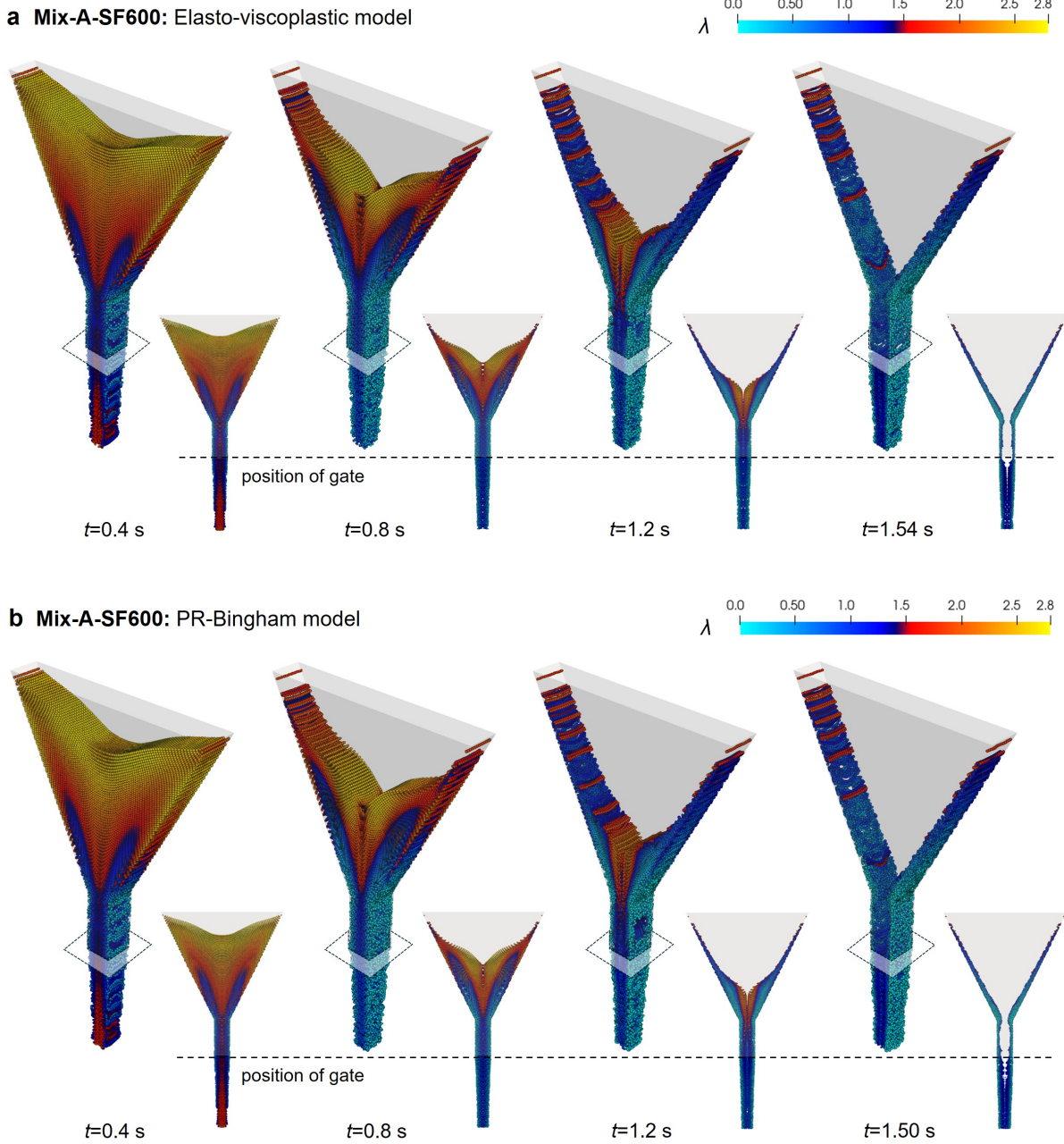


Figure 26: V-funnel test: Simulation results of Mix-A-SF600 using (a) the elasto-viscoplastic model and (b) the PR-Bingham model. Note that the last snapshot shows the results at  $T_v$ , the time until light can first be seen through the gate.

- Verification tests were performed to assess the model performance under pure flow conditions. In particular, a two-dimensional Poiseuille flow test verified that the proposed elasto-viscoplastic model and the regularized Bingham model yield essentially equivalent results under flowing conditions.
- The capabilities of the proposed model were further demonstrated through simulations of standard concrete tests, including slump flow, L-box, and V-funnel tests,

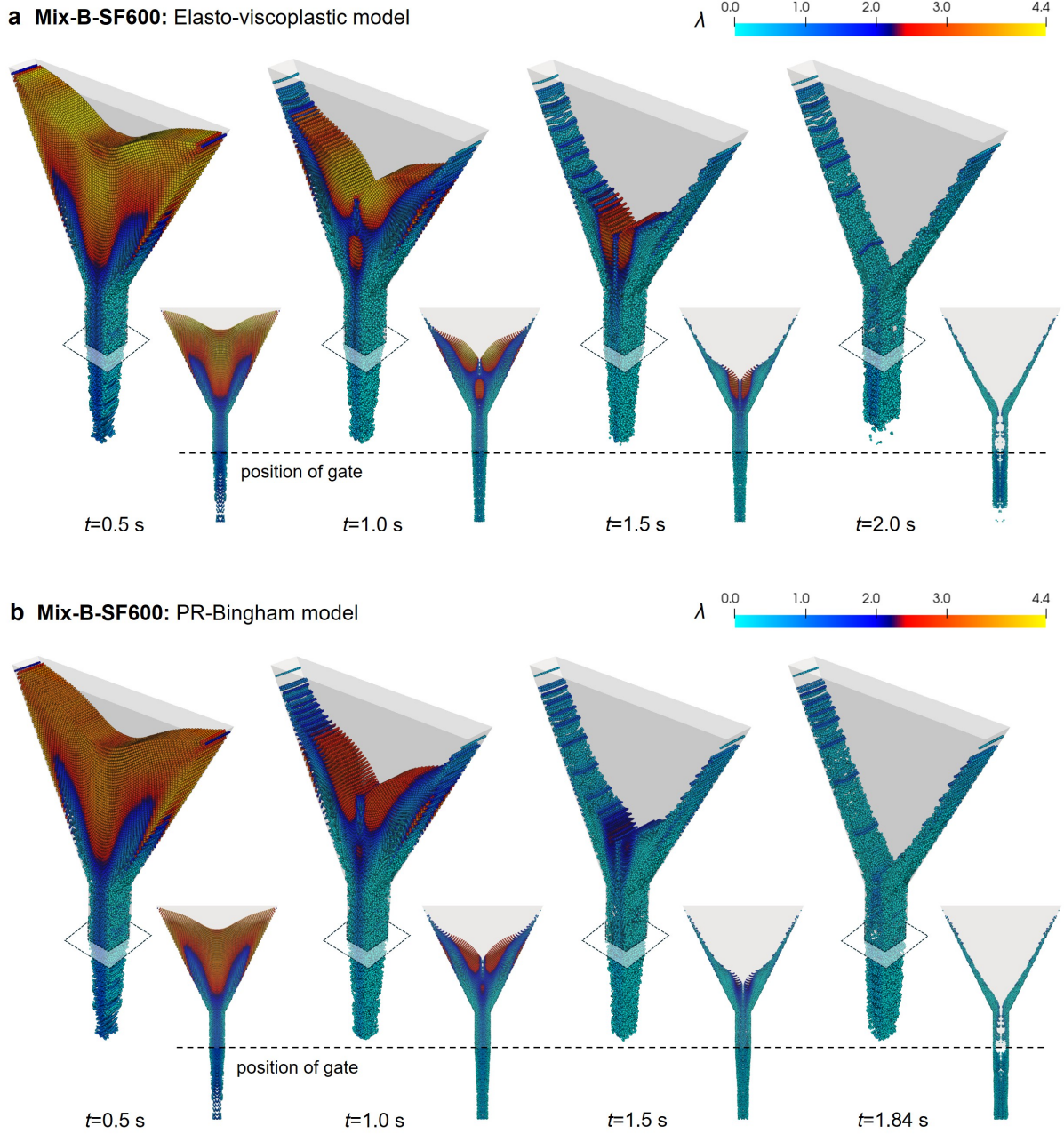


Figure 27: V-funnel test: Simulation results of Mix-B-SF600 using (a) the elasto-viscoplastic model and (b) the PR-Bingham model.

with results compared against the PR-Bingham model as well as existing analytical, numerical, and experimental results. The proposed model accurately captures the dynamic flow process, final runout distance, and cessation time. Upon stopping, the plastic shear rate reduces to zero, and the material transitions into an elastic response. In contrast, the PR-Bingham fluid model results in perpetual flow due to a non-vanishing shear rate, leading to unphysical overpredicted flow, such as ever-increasing slump diameters in slump flow tests and inaccurate final sur-

face profiles in L-box tests. Furthermore, a single set of thixotropic parameters successfully simulates concrete flow at different flocculation states, demonstrating parameter transferability across different test setups (e.g., from slump flow to L-box to V-funnel tests). The proposed model also captures the reduction of the flocculation state parameter,  $\lambda$ , during flow and its recovery during rest, as well as localized deflocculation induced by shear near obstacles such as rebars, which is crucial for simulating reinforced concrete flow in practical casting scenarios.

In summary, the elasto-viscoplastic thixotropic framework proposed in this study provides a physically consistent, numerically robust, and predictive tool for modeling the flow–rest transition in fresh concrete, addressing key limitations of fluid-based approaches. Despite these advancements, the model still has several limitations that suggest valuable directions for future research. First, the adopted Roussel thixotropy model, while practical, remains a simplification; incorporating more advanced microstructural evolution models could better separate and represent the effects of physical flocculation and chemical hydration. Second, more accurate boundary and interface modeling is needed to simulate flow around complex geometries and more realistic casting scenarios, such as congested reinforcement, which would benefit from improved boundary-condition imposition and contact algorithms capable of resolving the flow profile near interaction regions (Liang et al., 2023, 2024). Third, the model does not currently account for thermal effects, chemical reactions during resting, or concrete bleeding when water separates from the mixture; extending the framework to include thermo-hydro-chemo-mechanical couplings (Baumgarten and Kamrin, 2019; Yu et al., 2024c, 2025, 2026) would enable more comprehensive simulations of concrete behavior during casting and early-age curing.

### Declaration of competing interest

The authors declare that they have no known competing financial interests or personal relationships that could have appeared to influence the work reported in this paper.

### CRediT author contribution statement

**J. Yu:** Methodology, Software, Investigation, Validation, Formal analysis, Visualization, Writing - original draft. **B. Chandra:** Conceptualization, Methodology, Software, Investigation, Validation, Formal analysis, Visualization, Writing - original draft. **C. Wilkes:** Resources, Writing - review and editing. **J. Zhao:** Resources, Supervision, Writing - review and editing. **K. Soga:** Resources, Supervision, Writing - review and editing.

## Data availability

The data that support the findings of this study are available from the corresponding author upon reasonable request.

## Acknowledgements

The authors thank Dr. Hao Luo of the University of Cambridge for providing the experimental data presented in Section 4.1.2, and Chris Barker and Duncan Nicholson from Arup London for discussions on concrete modeling. J. Yu acknowledges the support of the Overseas Research Award from the Hong Kong University of Science and Technology for an exchange visit to the University of California, Berkeley. B. Chandra acknowledges Prof. Ken Kamrin of UC Berkeley for many enlightening discussions on topics related to plasticity theory and modeling.

## References

- Alyhya, W., Kulasegaram, S., Karihaloo, B., 2017. Simulation of the flow of self-compacting concrete in the v-funnel by sph. *Cement and Concrete Research* 100, 47–59.
- Amir, J., 2019. Honeycomb defects in concrete: Observations and solutions. [https://fernandeztadeo.com/Adobe/DFI\\_1905\\_Page\\_93-95.pdf](https://fernandeztadeo.com/Adobe/DFI_1905_Page_93-95.pdf). Accessed: 2025-11-16.
- Assaad, J., Khayat, K.H., Mesbah, H., 2003. Assessment of thixotropy of flowable and self-consolidating concrete. *Materials Journal* 100, 99–107.
- Barbhuiya, S., Kanavaris, F., Das, B.B., Idrees, M., 2024. Decarbonising cement and concrete production: Strategies, challenges and pathways for sustainable development. *Journal of building engineering* 86, 108861.
- Baumgarten, A.S., Kamrin, K., 2019. A general constitutive model for dense, fine-particle suspensions validated in many geometries. *Proceedings of the National Academy of Sciences* 116, 20828–20836.
- Beverly, C., Tanner, R., 1992. Numerical analysis of three-dimensional bingham plastic flow. *Journal of non-newtonian fluid mechanics* 42, 85–115.
- Bing, Y., Cortis, M., Charlton, T., Coombs, W., Augarde, C., 2019. B-spline based boundary conditions in the material point method. *Computers & Structures* 212, 257–274.
- Bingham, E.C., 1922. Fluidity and plasticity. McGraw-Hill Book Company, Incorporated.
- Bird, R.B., 2002. Transport phenomena. *Applied Mechanics Reviews* 55, R1–R4.
- Bird, R.B., Armstrong, R.C., Hassager, O., 1987. Dynamics of polymeric liquids. vol. 1: Fluid mechanics .
- Bolton, M., McKinley, J., 1997. Geotechnical properties of fresh cement grout—pressure filtration and consolidation tests. *Géotechnique* 47, 347–352.

- Brackbill, J., Ruppel, H., 1986. FLIP: A method for adaptively zoned, particle-in-cell calculations of fluid flows in two dimensions. *Journal of Computational physics* 65, 314–343.
- BSI, 2010. BS EN 12350-10:2010, Testing fresh concrete. Self-compacting concrete. L box test. Standard. British Standards Institute.
- BSI, 2010. BS EN 12350-9:2010, Testing fresh concrete – Self-compacting concrete. V-funnel test. British Standard. British Standards Institution.
- BSI, 2019. BS EN 12350-8:2019, Self Compacting concrete - Slump-flow test. Standard. British Standards Institute.
- Cai, Y., Liu, Q.f., Chen, M., Xiong, Q.X., Šavija, B., 2025. A cfd-based numerical model for predicting the slump and slump flow of fresh concrete from a rheological perspective. *Construction and Building Materials* 458, 138501.
- Cao, G., Li, Z., 2017. Numerical flow simulation of fresh concrete with viscous granular material model and smoothed particle hydrodynamics. *Cement and Concrete Research* 100, 263–274. doi:[10.1016/j.cemconres.2017.07.005](https://doi.org/10.1016/j.cemconres.2017.07.005).
- Chandra, B., Hashimoto, R., Kamrin, K., Soga, K., 2024a. Mixed material point method formulation, stabilization, and validation for a unified analysis of free-surface and seepage flow. *Journal of Computational Physics* 519, 113457.
- Chandra, B., Hashimoto, R., Matsumi, S., Kamrin, K., Soga, K., 2024b. Stabilized mixed material point method for incompressible fluid flow analysis. *Computer Methods in Applied Mechanics and Engineering* 419, 116644.
- Chandra, B., Singer, V., Teschemacher, T., Wuechner, R., Larese, A., 2021. Nonconforming dirichlet boundary conditions in implicit material point method by means of penalty augmentation. *Acta Geotechnica* , 1–21.
- Chhabra, R.P., Patel, S.A., 2025. Non-Newtonian flow and applied rheology: engineering applications. Elsevier.
- Civil Engineer Mag, 2025. Honeycombing in concrete: Causes & fixes. <https://www.civilengineermag.com/honeycombing-in-concrete/>. Accessed: 2025-11-16.
- Comminal, R., Da Silva, W.R.L., Andersen, T.J., Stang, H., Spangenberg, J., 2020. Modelling of 3d concrete printing based on computational fluid dynamics. *Cement and Concrete Research* 138, 106256.
- Comminal, R., Serdeczny, M.P., Pedersen, D.B., Spangenberg, J., 2018. Numerical modeling of the strand deposition flow in extrusion-based additive manufacturing. *Additive Manufacturing* 20, 68–76.
- De Schryver, R., El Cheikh, K., Lesage, K., De Schutter, G., 2018. Cfd implementation of time-dependent behaviour: application for concrete pumping, in: *Symposium on Concrete Modelling (CONMOD2018)*, Netherlands, Delft, pp. 122–130.
- De Vaucorbeil, A., Nguyen, V.P., Sinaie, S., Wu, J.Y., 2020. Material point method after 25 years: Theory, implementation, and applications. *Advances in applied mechanics* 53, 185–398.

- Deeb, R., Kulasegaram, S., Karihaloo, B., 2014. 3d modelling of the flow of self-compacting concrete with or without steel fibres. part i: slump flow test. *Computational Particle Mechanics* 1, 373–389.
- Desai, J., 2025. Concrete honeycombing – causes, effects, and prevention tips. <https://gharpedia.com/blog/concrete-honeycombing/>. Accessed: 2025-11-16.
- Ding, X., Jia, W., Li, C., Geng, H., Chen, G., Zhao, S., 2025. Study on the meso-scale numerical simulation method for flow behavior of fresh self-compacting steel fiber reinforced concrete based on dem-sph coupling. *Construction and Building Materials* 496, 143804.
- Domone, P., 1998. The slump flow test for high-workability concrete. *Cement and Concrete Research* 28, 177–182.
- Dunatunga, S., Kamrin, K., 2015. Continuum modelling and simulation of granular flows through their many phases. *Journal of Fluid Mechanics* 779, 483–513.
- Elop Technology, 2023. Detection of honeycombing by elop insight scanner. <https://elop.no/detection-of-honeycombing/>. Accessed: 2025-11-16.
- Environment, U., Scrivener, K.L., John, V.M., Gartner, E.M., 2018. Eco-efficient cements: Potential economically viable solutions for a low-co2 cement-based materials industry. *Cement and concrete Research* 114, 2–26.
- Ferron, R.D., Shah, S., Fuente, E., Negro, C., 2013. Aggregation and breakage kinetics of fresh cement paste. *Cement and Concrete Research* 50, 1–10.
- Feys, D., Khayat, K., 2018. Testing concrete for deep foundations. final report, Missouri University of Science and Technology, Rolla, MO .
- Geuzaine, C., Remacle, J.F., 2009. Gmsh: A 3-d finite element mesh generator with built-in pre-and post-processing facilities. *International journal for numerical methods in engineering* 79, 1309–1331.
- Herschel, W.H., Bulkley, R., 1926. Konsistenzmessungen von gummi-benzollösungen. *Kolloid-Zeitschrift* 39, 291–300.
- Hughes, T.J., 1980. Generalization of selective integration procedures to anisotropic and nonlinear media. *International Journal for Numerical Methods in Engineering* 15, 1413–1418.
- Jasak, H., Jemcov, A., Tukovic, Z., et al., 2007. Openfoam: A c++ library for complex physics simulations, in: International workshop on coupled methods in numerical dynamics, Dubrovnik, Croatia). pp. 1–20.
- Jiao, D., De Schryver, R., Shi, C., De Schutter, G., 2021. Thixotropic structural build-up of cement-based materials: A state-of-the-art review. *Cement and Concrete Composites* 122, 104152.
- Kränel, T., 2018. Rheology and workability testing of deep foundation concrete, in: Internationale Conference on Deep Foundations and Ground Improvement.
- Kularathna, S., Liang, W., Zhao, T., Chandra, B., Zhao, J., Soga, K., 2021. A semi-implicit material point method based on fractional-step method for saturated soil. *International Journal for Numerical and Analytical Methods in Geomechanics* 45, 1405–1436.

- Kumar, R., 2023. Honeycomb in concrete: Causes, prevention, and repairing. <https://civilengineerdk.com/honeycomb-in-concrete/>. Accessed: 2025-11-16.
- Kurima, J., Chandra, B., Soga, K., 2025. Absorbing boundary conditions in material point method adopting perfectly matched layer theory. *Soil Dynamics and Earthquake Engineering* 191, 109219.
- Lecompte, T., Perrot, A., 2017. Non-linear modeling of yield stress increase due to scc structural build-up at rest. *Cement and Concrete Research* 92, 92–97.
- Li, Y., Mu, J., Wang, Z., Liu, Y., Du, H., 2021. Numerical simulation on slump test of fresh concrete based on lattice boltzmann method. *Cement and Concrete Composites* 122, 104136.
- Li, Z., Zhou, X., Ma, H., Hou, D., 2022. Advanced concrete technology. John Wiley & Sons.
- Liang, W., Fang, H., Yin, Z.Y., Zhao, J., 2024. A mortar segment-to-segment frictional contact approach in material point method. *Computer Methods in Applied Mechanics and Engineering* 431, 117294.
- Liang, Y., Chandra, B., Soga, K., 2022. Shear band evolution and post-failure simulation by the extended material point method (xmpm) with localization detection and frictional self-contact. *Computer Methods in Applied Mechanics and Engineering* 390, 114530.
- Liang, Y., Given, J., Soga, K., 2023. The imposition of nonconforming neumann boundary condition in the material point method without boundary representation. *Computer methods in applied mechanics and engineering* 404, 115785.
- Lowke, D., 2018. Thixotropy of scc—a model describing the effect of particle packing and superplasticizer adsorption on thixotropic structural build-up of the mortar phase based on interparticle interactions. *Cement and Concrete Research* 104, 94–104.
- Luo, H., 2014. Experimental and Numerical Investigation on Fresh Cement Deformation Behaviour. Master's thesis. University of Cambridge.
- Macdonald, J.R., 1966. Some simple isothermal equations of state. *Reviews of Modern Physics* 38, 669.
- Mahaut, F., Mokéddem, S., Chateau, X., Roussel, N., Ovarlez, G., 2008. Effect of coarse particle volume fraction on the yield stress and thixotropy of cementitious materials. *Cement and concrete research* 38, 1276–1285.
- Mahjoubi, S., Sun, M., Lin, C., 2025. Thermal integrity profiling of cast-in-place piles with defects: Insights from numerical modeling. *Journal of Geotechnical and Geoenvironmental Engineering* 151, 04025089.
- Manica, R., De Bortoli, A., 2004. Simulation of sudden expansion flows for power-law fluids. *Journal of Non-Newtonian Fluid Mechanics* 121, 35–40.
- Martinello, N., 2018. Geotechnical engineering and honeycombing issues in concrete. [https://associazionegeotecnica.it/wp-content/uploads/2018/11/RIG\\_3\\_2018\\_066\\_-MARTINELLO.pdf](https://associazionegeotecnica.it/wp-content/uploads/2018/11/RIG_3_2018_066_-MARTINELLO.pdf). Accessed: 2025-11-16.
- Megid, W.A., Khayat, K.H., 2018. Effect of concrete rheological properties on quality of formed surfaces cast with self-consolidating concrete and superworkable concrete. *Cement and Concrete Composites* 93, 75–84.

- Mitchell, T., Barker, C., Wilkes, C., Li, C., 2025. Investigating the unseen flow of concrete in deep foundation construction doi:[10.37308/DFIEFFC25630211](https://doi.org/10.37308/DFIEFFC25630211).
- Mu, J., Li, Y., Hao, J., Liu, Y., Shen, J., 2023. Research on discrete element simulation of slump test for fresh self-compacting concrete. *Journal of Building Engineering* 70, 106464.
- Mu, J., Li, Y., Jin, C., Liu, Y., Li, H., Liu, J., 2022. Simulation of v-tunnel test for fresh concrete on the basis of lattice boltzmann method. *Cement and Concrete Composites* 133, 104728.
- Nairn, J.A., 2003. Material point method calculations with explicit cracks. *Computer Modeling in Engineering and Sciences* 4, 649–664.
- Nan, X., Wang, Z., Hou, J., Tong, Y., Li, B., 2021. Clogging mechanism of pervious concrete: From experiments to cfd-dem simulations. *Construction and Building Materials* 270, 121422.
- Nguyen, T., Roussel, N., Coussot, P., 2006. Correlation between l-box test and rheological parameters of a homogeneous yield stress fluid. *Cement and Concrete Research* 36, 1789–1796.
- Nilimaa, J., 2023. Smart materials and technologies for sustainable concrete construction. *Developments in the Built Environment* 15, 100177.
- O'donovan, E., Tanner, R., 1984. Numerical study of the bingham squeeze film problem. *Journal of Non-Newtonian fluid mechanics* 15, 75–83.
- Ouyang, Z., Yu, Z., Khoo, B.C., Wang, D., Phan-Thien, N., 2022. A hybrid smoothed particle hydrodynamics coupled to a fictitious domain method for particulate flows and its application in a three-dimensional printing process. *Journal of Computational Physics* 463, 111312.
- Papanastasiou, T.C., 1987. Flows of materials with yield. *Journal of rheology* 31, 385–404.
- Perrot, A., Rangeard, D., Pierre, A., 2016. Structural built-up of cement-based materials used for 3d-printing extrusion techniques. *Materials and Structures* 49, 1213–1220.
- Pichler, C., Röck, R., Lackner, R., 2017. Apparent power-law fluid behavior of vibrated fresh concrete: Engineering arguments based on stokes-type sphere viscometer measurements. *Journal of Non-Newtonian Fluid Mechanics* 240, 44–55.
- Qian, Y., Kawashima, S., 2016. Flow onset of fresh mortars in rheometers: Contribution of paste deflocculation and sand particle migration. *Cement and concrete research* 90, 97–103.
- Rao, A.R., Mishra, M., 2004. Peristaltic transport of a power-law fluid in a porous tube. *Journal of Non-Newtonian Fluid Mechanics* 121, 163–174.
- Reinold, J., Meschke, G., 2022. A mixed u–p edge-based smoothed particle finite element formulation for viscous flow simulations. *Computational Mechanics* 69, 891–910. doi:[10.1007/s00466-021-02119-w](https://doi.org/10.1007/s00466-021-02119-w).
- Roussel, N., 2005. Steady and transient flow behaviour of fresh cement pastes. *Cement and concrete research* 35, 1656–1664.
- Roussel, N., 2006a. A thixotropy model for fresh fluid concretes: Theory, validation and applications. *Cement and Concrete Research* 36, 1797–1806.

- Roussel, N., 2006b. A thixotropy model for fresh fluid concretes: Theory, validation and applications. *Cement and Concrete Research* 36, 1797–1806. doi:[10.1016/j.cemconres.2006.05.025](https://doi.org/10.1016/j.cemconres.2006.05.025).
- Roussel, N., Coussot, P., 2005. “fifty-cent rheometer” for yield stress measurements: from slump to spreading flow. *Journal of rheology* 49, 705–718.
- Roussel, N., Geiker, M.R., Dufour, F., Thrane, L.N., Szabo, P., 2007. Computational modeling of concrete flow: General overview. *Cement and Concrete Research* 37, 1298–1307. doi:[10.1016/j.cemconres.2007.06.007](https://doi.org/10.1016/j.cemconres.2007.06.007).
- Roussel, N., Gram, A., Cremonesi, M., Ferrara, L., Krenzer, K., Mechtcherine, V., Shyshko, S., Skocec, J., Spangenberg, J., Svec, O., Thrane, L.N., Vasilic, K., 2016a. Numerical simulations of concrete flow: A benchmark comparison. *Cement and Concrete Research* 79, 265–271. doi:[10.1016/j.cemconres.2015.09.022](https://doi.org/10.1016/j.cemconres.2015.09.022).
- Roussel, N., Gram, A., Cremonesi, M., Ferrara, L., Krenzer, K., Mechtcherine, V., Shyshko, S., Skocec, J., Spangenberg, J., Svec, O., et al., 2016b. Numerical simulations of concrete flow: A benchmark comparison. *Cement and Concrete Research* 79, 265–271.
- Roussel, N., Ovarlez, G., Garrault, S., Brumaud, C., 2012a. The origins of thixotropy of fresh cement pastes. *Cement and Concrete Research* 42, 148–157. doi:[10.1016/j.cemconres.2011.09.004](https://doi.org/10.1016/j.cemconres.2011.09.004).
- Roussel, N., Ovarlez, G., Garrault, S., Brumaud, C., 2012b. The origins of thixotropy of fresh cement pastes. *Cement and concrete research* 42, 148–157.
- Shin, T.Y., Kim, J.H., 2023. Flow simulation of fresh concrete accounting for vibrating compaction. *Cement and Concrete Research* 173, 107300.
- Simo, J.C., Hughes, T.J., 2006. Computational inelasticity. volume 7. Springer Science & Business Media.
- Soga, K., Alonso, E., Yerro, A., Kumar, K., Bandara, S., 2016. Trends in large-deformation analysis of landslide mass movements with particular emphasis on the material point method. *Géotechnique* 66, 248–273. doi:[10.1680/jgeot.15.LM.005](https://doi.org/10.1680/jgeot.15.LM.005).
- Suiker, A.S., Wolfs, R.J., Lucas, S.M., Salet, T.A., 2020. Elastic buckling and plastic collapse during 3d concrete printing. *Cement and Concrete Research* 135, 106016.
- Sulsky, D., Chenb, Z., Schreyer, H.L., 1994. A particle method for history-dependent materials. *Computer Methods in Applied Mechanics and Engineering* 118, 179–196.
- Sun, Q., Elshafie, M., Barker, C., Fisher, A., Schooling, J., Rui, Y., 2021. Thermal integrity testing of cast in situ piles: An alternative interpretation approach. *Structural Health Monitoring* 20, 2493–2512.
- Sun, Q., Elshafie, M.Z., Xu, X., Schooling, J., 2024. Pile defect assessment using distributed temperature sensing: fundamental questions examined. *Structural Health Monitoring* 23, 1701–1724.
- Tao, Y., Chen, X., Zhang, Y., De Schryver, R., Jiang, W., 2024. Modeling thixotropic behavior of fresh cement pastes. *Materials Letters* 371, 136884.
- Thanh, H.T., Li, J., Zhang, Y., 2020. Numerical simulation of self-consolidating engineered cementitious composite flow with the v-funnel and u-box. *Construction and Building Materials* 236, 117467.

- Thiedeitz, M., Habib, N., Kränkel, T., Gehlen, C., 2020. L-box form filling of thixotropic cementitious paste and mortar. *Materials* 13, 1760.
- Thiedeitz, M., Thimothy, J.J., 2024. Time-dependent flow simulation of thixotropic cementitious pastes, in: Proceedings of the 9th European Congress on Computational Methods in Applied Sciences and Engineering (ECCOMAS Congress 2024), Lisbon, Portugal.
- Wallevik, J.E., 2009. Rheological properties of cement paste: Thixotropic behavior and structural breakdown. *Cement and concrete research* 39, 14–29.
- Wallevik, O.H., Feys, D., Wallevik, J.E., Khayat, K.H., 2015. Avoiding inaccurate interpretations of rheological measurements for cement-based materials. *Cement and Concrete Research* 78, 100–109.
- Wallevik, O.H., Wallevik, J.E., 2011. Rheology as a tool in concrete science: The use of rheographs and workability boxes. *Cement and concrete research* 41, 1279–1288.
- Wilkes, C., Kanavaris, F., Barker, C., Nicholson, D., 2024. Practical recommendations for defect avoidance in deep foundations. *ACI Materials Journal* 121.
- Wilkes, C., Kumar, K., Biscontin, G., 2023. Investigating the thixotropic behaviour of Tremie Concrete using the Slump-flow test and the Material Point Method. *Cement and Concrete Composites* 143, 105222. doi:[10.1016/j.cemconcomp.2023.105222](https://doi.org/10.1016/j.cemconcomp.2023.105222).
- Wu, J., Jia, Z., Zhou, X., 2023. Discrete element analysis of the effect of aggregate morphology on the flowability of self-compacting concrete. *Case Studies in Construction Materials* 18, e02010.
- Ye, H., Zhang, J., Gao, X., Ling, J., Zhu, X., Jiao, D., 2024. Showing the role of weakly-bound particles flocculation in the reversibility of thixotropic behavior for fresh cement paste. *Construction and Building Materials* 411, 134624.
- Yildizdag, M.E., 2024. Numerical modeling and simulation of material extrusion-based 3-d printing processes with a material point method framework. *Continuum Mechanics and Thermodynamics* 36, 1361–1378.
- Yu, H., Zhang, W., Yin, B., Sun, W., Akbar, A., Zhang, Y., Liew, K.M., 2024a. Modeling extrusion process and layer deformation in 3D concrete printing via smoothed particle hydrodynamics. *Computer Methods in Applied Mechanics and Engineering* 420, 116761. doi:[10.1016/j.cma.2024.116761](https://doi.org/10.1016/j.cma.2024.116761).
- Yu, J., Weijian, L., Zhao, J., 2025. Enhancing dynamic modeling of porous media with compressible fluid: A thm material point method with improved fractional step formulation. *Computer Methods in Applied Mechanics and Engineering* 444. doi:[10.1016/j.cma.2025.118100](https://doi.org/10.1016/j.cma.2025.118100).
- Yu, J., Zhao, J., Liang, W., Zhao, S., 2024b. Multiscale modeling of coupled thermo-hydro-mechanical behavior in ice-bonded granular media subject to freeze-thaw cycles. *Computers and Geotechnics* 171, 106349. doi:[10.1016/j.compgeo.2024.106349](https://doi.org/10.1016/j.compgeo.2024.106349).
- Yu, J., Zhao, J., Liang, W., Zhao, S., 2024c. A semi-implicit material point method for coupled thermo-hydro-mechanical simulation of saturated porous media in large deformation. *Computer Methods in Applied Mechanics and Engineering* 418, 116462. doi:[10.1016/j.cma.2023.116462](https://doi.org/10.1016/j.cma.2023.116462).

Yu, J., Zhao, J., Soga, K., Zhao, S., Liang, W., 2026. A fully coupled thmc-mpm framework for modeling phase transition and large deformation in methane hydrate-bearing sediment. *Journal of Mechanics Physics of Solids* 206, 106368. doi:[10.1016/j.jmps.2025.106368](https://doi.org/10.1016/j.jmps.2025.106368).

Yu, J., Zhao, J., Zhao, S., Liang, W., 2024d. Thermo-hydro-mechanical coupled material point method for modeling freezing and thawing of porous media. *International Journal for Numerical and Analytical Methods in Geomechanics* 48, 3308–3349. doi:[10.1002/nag.3794](https://doi.org/10.1002/nag.3794).

Yue, Y., Smith, B., Batty, C., Zheng, C., Grinspun, E., 2015. Continuum foam: A material point method for shear-dependent flows. *ACM Transactions on Graphics (TOG)* 34, 1–20.

Zhang, X., Chen, Z., Liu, Y., 2016. The material point method: a continuum-based particle method for extreme loading cases. Academic Press.